Institute for Atmospheric and Climate Science
ETH Zurich, Switzerland

Diploma Thesis

On the Melt Water Production due to Strain Heating in Storglaciären, Sweden

Andy Aschwanden

SS 2004

Supervisor: Prof. Heinz Blatter

Zusammenfassung

Storglaciären ist ein polythermaler Gletscher in Lappland, Nordschweden, welcher sich besonders gut für Modell- und Prozessstudien eignet, da er zu den bestuntersuchtesten Gletschern der Welt gehört und eine grosse Menge an gemessenen Daten vorhanden ist.

Der Gehalt von flüssigem Wasser in temperiertem Eis ist wichtig für das Fliessverhalten des Gletschers sowie auch für die Stabilität der Temperaturschichtung bei polythermalen Gletschern. Eine von vier möglichen Ursachen für das Auftreten von Wasser in temperiertem Eis ist die Schmelzwasserproduktion aufgrund der Deformationswärme. In der vorliegenden Diplomarbeit wird die Deformationswärme innerhalb der temperierten Schicht berechnet und der daraus resultierende Wassergehalt an der Übergangsschicht zwischen kaltem und temperiertem Eis bestimmt. Der erhaltene Wert von $0.0006\,\mathrm{kg_w/kg}$ erscheint plausibel und stimmt gut mit einer groben Abschätzung von $0.001\,\mathrm{kg_w/kg}$ von Pettersson et al. (2004) überein.

Um das Geschwindigkeitsfeld zu berechnen, wurde ein zweidimensionales Gletschermodell verwendet, das auch Terme zweiter Ordnung einbezieht. Vergleiche mit Berechnungen basierend auf einer Approximation erster Ordnung zeigen deutliche Unterschiede auf: Wird ein für den ganzen Gletscher konstanter und für beide Ordnungen gleicher Deformationsparameter verwendet, sind die berechneten Geschwindigkeiten des Zweitordnungsmodells durchgehend grösser. Da der Programmcode für das Zweitordnungsmodell neu und bisher ungetestet ist, wird ein Programmierfehler im Code vermutet. Um ein möglichst realistisches und mit gemessenen Oberflächengeschwindigkeiten übereinstimmendes Geschwindigkeitsfeld zu simulieren, wird ein neuer Weg bestritten: Der Deformationsparameter wird in longitudinaler Richtung solange iterativ angepasst, bis die berechneten Oberflächengeschwindigkeiten mit den gemessenen übereinstimmen. Mit dem daraus erhaltenen Fliessfeld werden Trajektorien gerechnet und anschliessend die Schmelzwasserproduktion aufgrund von Deformationswärme bestimmt. Tests mit verschiedenen basalen Gleitgeschwindigkeiten deuten auf die Existenz einer temperierten, aber fast wasserfreien Zone direkt unter der kalten Schicht hin.

Abstract

Storglaciären, a polythermal glacier in Lappland, northern Sweden, is a particulary well suited glacier for all types of model and process studies thanks to a wealth of available data.

The content of liquid water in temperate ice is important for the flow of glaciers as well as for the stability of the thermal layering in polythermal glaciers (Pettersson et al., 2004). One of four possible sources for liquid water is melting due to strain heating. In this diploma thesis, strain heating in the temperate layer of Storglaciären is calculated. Following this, the water content due to strain heating is assessed along the cold-temperate transition surface. A mean value of $0.0006\,\mathrm{kg_w/kg}$ in the proximity of three thermistor strings is presented which complies with a rough estimate of $0.001\,\mathrm{kg_w/kg}$ by Pettersson et al. (2004) for the same region.

A second order ice flow model was used to calculate velocity fields. The results yield much higher velocities throughout the entire glacier compared to first order model results. A dependence of the rate factor on the numerical order is assumed. Additionally, the zero surface traction boundary condition was reproduced worse. A hidden error in the program code is suspected. Due to the need for a velocity field as close to observed surface data as possible, an novel approach was chosen: The rate factor was allowed to vary in longitudinal direction. The model was tuned in a way such that it reproduces surface velocities in close agreement with prescribed surface velocities. Flow lines were calculated and the melt water production due to strain heating assessed.

Tests with an alternative basal velocity boundary condition suggest the existence of a temperate, but dry zone within the glacier.

Contents

1 Introduction **1**
1.1 Motivation . . . 1
1.2 Objectives . . . 1
1.3 Outline . . . 1

2 Storglaciären **3**
2.1 Physical Description . . . 4
2.2 Previous Work on Storglaciären and in the Tarfala Valley . . . 4
2.3 Observations . . . 7
2.3.1 Surface and Bed Topography and Position of the CTS . . . 7
2.3.2 Ice Velocity . . . 7
2.3.3 Water Content . . . 10

3 Models and Model Tests **11**
3.1 Second Order Ice Flow Model . . . 11
3.1.1 Governing Equations . . . 11
3.1.2 Model Description . . . 13
3.1.3 Tests with a Constant Rate Factor . . . 13
3.1.4 Tests with Prescribed Basal and Surface Velocity . . . 20
3.2 Trajectory Model . . . 28
3.2.1 Model Description . . . 28
3.2.2 Test of Trajectory Model . . . 28

4 Strain Heating and Water Content **35**
4.1 Strain Heating . . . 35
4.2 Melt Water Production . . . 36

5 Conclusions and Prospects **38**

6 Acknowledgments **39**

Bibliography **40**

List of Figures

2.1 Schematic view of different polythermal structures 5
2.2 Location of Storglaciären 6
2.3 Map of Storglaciären and slice along the *kinematic center line* 8
2.4 Velocity stake net 9
2.5 Location map of GPR profiles and interpolated water content. 10

3.1 Comparsion of velocity fields with constant rate factor 16
3.2 Surface velocities using a constant rate factor 17
3.3 Accumulation function and surface traction using a constant rate factor . 18
3.4 Stress fields with constant rate factor 19
3.5 Prescribed basal and surface boundary conditions 21
3.6 Prescribed basal and surface boundary conditions and rate factors after tuning. 23
3.7 Velocity fields with prescribed basal and surface velocity 24
3.8 Surface velocities using prescribed basal and surface velocity 25
3.9 Stress fields with prescribed basal and surface velocity 26
3.10 Accumulation function and surface traction. 27
3.11 Trajectories 29
3.12 Selected trajectories 29
3.13 Accuracy test of the forward Euler scheme 31
3.14 Tests with an alternative basal velocity boundary condition. 32
3.15 Schematic depiction of the difference between the cold-temperate transition surface and the wet-dry transition surface. 34

4.1 Water content due to strain heating. 37

List of Tables

3.1 Model setup used for tests with a constant rate factor 13
3.2 Model configurations 14
3.3 Comparison of 1st and 2nd-order velocity fields a with constant rate factor 15
3.4 Model setup used for tests with prescribed basal and surface velocities . . 21
3.5 Comparison of 1st and 2nd-order velocity fields with prescribed basal and surface velocity. 22
3.6 General properties of trajectories 28
3.7 Numerical tests with trajectories 30
3.8 Trajectory comparison sheet 33

1 Introduction

1.1 Motivation

R. Pettersson studied the *dynamics of the cold surface layer of polythermal Storglaciären, Sweden* in his Ph.D. thesis (Pettersson, 2004). Among other things, he investigated the spatial variability in water content at the *cold-temperate transition surface* (CTS) which led to a publication in the *Journal of Geophysical Research* (Pettersson et al., 2004). Ground-penetrating radar measurements were made and results calibrated with direct measurements at three thermistor strings using a novel field experiment proposed by H. Blatter. Four different sources of liquid water were compared and a rough estimate of the water content due to strain heating was given. However, many questions were left unanswered.

1.2 Objectives

This work aims at verifying the rough estimate given by Pettersson et al. (2004). To accomplish this, an elaborate scheme was chosen. A second order ice flow model is used to produce a velocity field, which in turn, is used to model flow lines. Then, strain heating and the resulting water content is calculated.

1.3 Outline

Chapter 2 introduces glaciers with a polythermal temparture regime. The site of study is presented and a short summary of previous work is given. Measurements that build the basis of this work are discussed.

Chapter 3 focuses on numerical models and model tests. Governing equations are briefly introduced and the chosen boundary conditions are justified. All essential steps in order to come up with a realistic velocity field and reasonable flow lines are explained in detail and results are discussed.

Chapter 4 points out how strain heating and melt water resulting from strain heating is calculated. The distribution of water due to strain heating within the temperate layer is shown, as well as the water content due to strain heating along the transition surface between the cold and the temperate layer. Results are compared to those presented by R. Pettersson.

Chapter 5 summarizes the results and gives an outlook to future work.

2 Storglaciären

The term *polythermal glacier* was first introduced by Fowler and Larson (1978). Polythermal glaciers consist of both temperate ice (i.e. ice at the pressure melting point) and cold ice (i.e. ice below the pressure melting point). Temperate ice is characterized by the occurence of liquid water within the ice. Four different sources are assumed to be the origin for liquid water in glaciers (Paterson, 1971; Lliboutry, 1976):

1. water trapped in the ice as water-filled pores close-off at the firn-ice transition in the accumulation area
2. melting due to strain heating
3. water entering the glacier at the surface
4. adjustment of the pressure melting point due to changes in overburden pressure heats or cools temperate ice. The energy is balanced by freezing or melting of liquid water within the ice

The content of liquid water can differ remarkably between different glaciers, estimates range from 0 % to 9 %; an overview of water content determinations for various glaciers is given in Pettersson et al. (2004). On the other hand, cold ice is free of liquid water. The CTS represents a surface of phase change. Water arriving at the CTS freezes immediately and the released energy is transported into the cold ice through a nonvanishing temperature gradient (Greve, 1995).

Blatter and Hutter (1991) identified five different thermal structures in polythermal glaciers and Blatter (1991) added a sixth. Glaciers with a thermal layering as in Figures 2.1(a) and 2.1(b) are found in cold regions. The bulk of ice is cold except for a temperate layer near the bed which exists due to melt water resulting from strain heating. Figure 2.1(c) illustrates a glacier where the lower part of the accumulation area experiences high melting in spring and summer. This melt water infiltrates the firn pack. Refreezing at the transition to the cold firn produces latent heat that warms up the firn until it becomes temperate and allows for formation of temperate ice within an otherwise cold glacier. In the European Alps at high altitudes and on small Greenlandic ice caps, glaciers of the type shown in Figure 2.1(d) can be found (Haeberli, 1976). Figure 2.1(e) illustrates a polythermal structure commonly found on Svalbard and on the eastern side of the Scandinavian mountains (Pettersson, 2004, and references therein). This type is sometimes called *Scandinavian*-type or *Svalbard*-type. High net ablation at lower altitudes can turn the cold ice into temperate ice, while the cold layer can still exist higher up (Figure 2.1(f)).

Polythermal glaciers can be found mainly at high latitudes (Hutter et al., 1988), but also at high altitudes in the European Alps (Haeberli, 1976) and in China (Maohuan, 1990).

2.1 Physical Description

The following brief overview is a summary taken from Holmlund and Jansson (2001) and slightly modified:

Storglaciären (67°55′ N, 18°35′ E) is a small glacier located on the eastern side of the Kebnekaise massif in Lappland, northern Sweden (Figure 2.2). The length of the glacier is 3.2 km from its head at $\sim$ 1730 m a.s.l. to the terminus at $\sim$ 1120 m a.s.l. and has a total surface area of 3 km^2. There are four over-deepened areas in the bed, which would result in four small lakes if the glacier would disappear. The largest of these over-deepenings is located beneath the upper part of the ablation area, and has a depression of 50 m. The accumulation area consists of two cirque-type basins, a larger one to the north contributing the major portion of the flow, and a smaller one to the south. The glacier has an average ice thickness of 95 m, with a maximum depth of 250 m in the upper part of the ablation area.

Storglaciären is a polythermal glacier of the type depicted in Figure 2.1(e). The bulk is temperate ($\sim$ 85%), but the surface layer of the ablation area is cold. The average thickness of the cold layer is 31 m, with a maximum thickness of 65 m along the southern margin, decreasing towards the approximate position of the equilibrium line. The surface layer of the accumulation area is only cold seasonally.

2.2 Previous Work on Storglaciären and in the Tarfala Valley

The first scientific studies on Storglaciären started in the mid 1940s and were made by Walter Schytt on the initiation of Professor Hans W. Ahlmann. Since then, a wealth of data has been collected. The Tarfala Research Station is the basis of all research done in and around the Tarfala Valley. It was established during the years 1947-49 and continuously expanded since then. Today, Tarfala Research Station is an important and well known site for glaciology-related research. Continuous mass balance measurements began in 1945, but measurement techniques and methods varied in the 1940s and 1950s and it was not until 1965 when mass balance measurements started according to a fixed scheme (Holmlund et al., 1996). Scientific research in Tarfala is not limited to glaciology alone, there is also a strong focus on meteorology and climatology, especially on glacier-climate interaction. Since 1995, Tarfala has been part of the official network of meteorological stations maintained by the Swedish Meteorological and Hydrological Institute (SMHI). Summer air temperature (JJA) measurements began in 1946 and the first automatic wheather station was installed in 1965, allowing continuous data

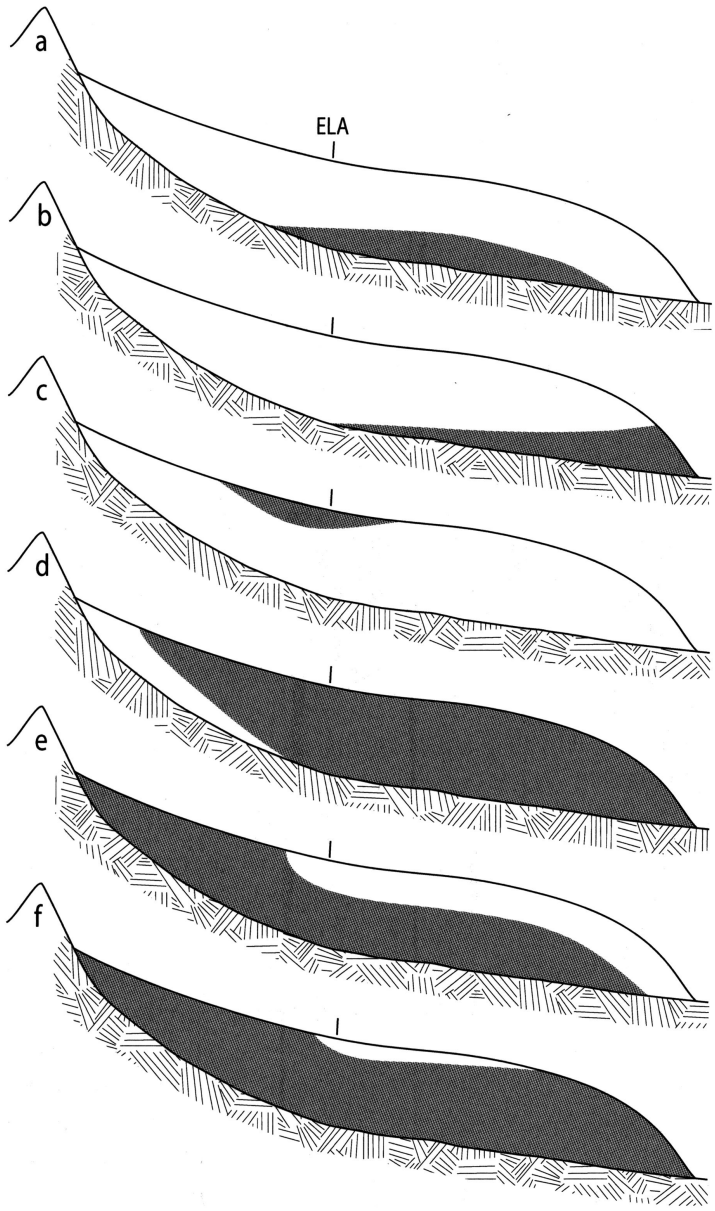

Figure 2.1: Schematic view of different polythermal structures based on Blatter and Hutter (1991) and modified by Pettersson (2004). The gray color indicates temperate ice and the equilibrium line altitude (ELA) is indicated with a line. Courtesy of R. Pettersson.

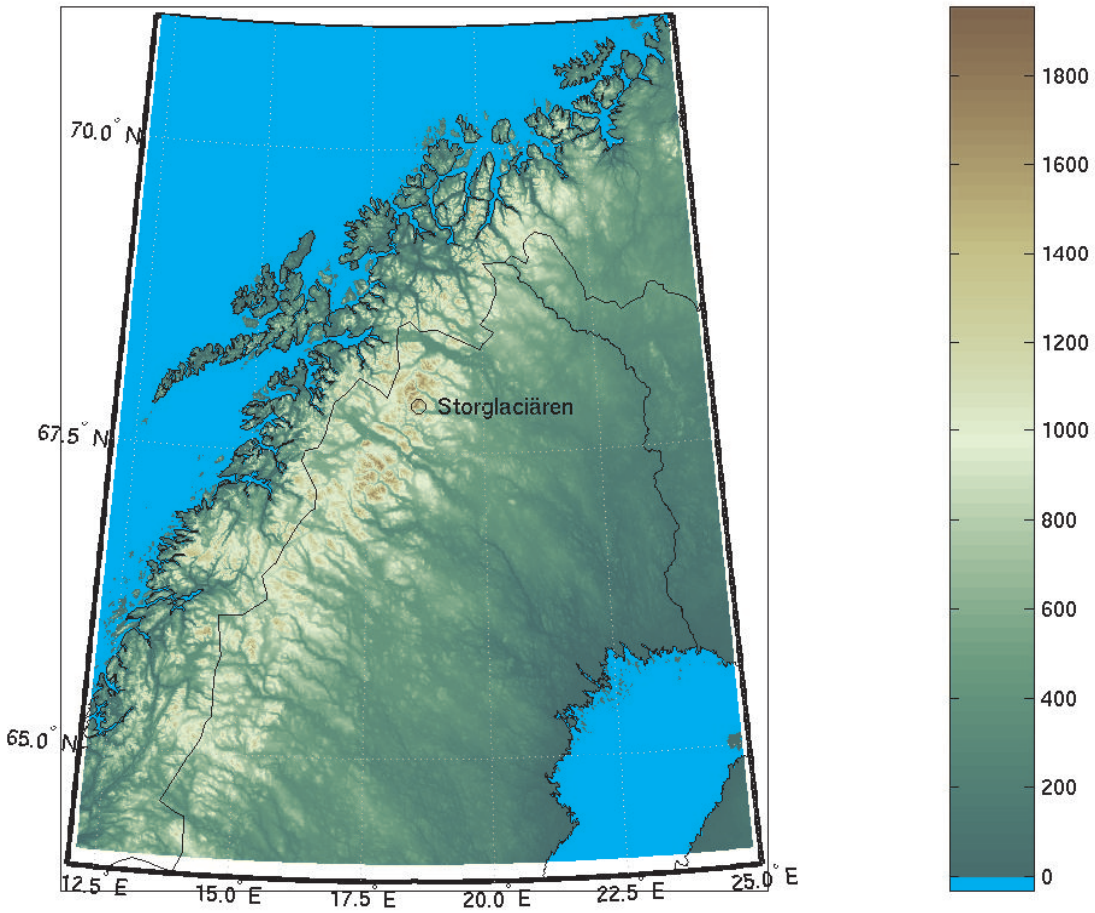

Figure 2.2: Location of Storglaciären. Colors indicates meters above sea level.

collection throughout the year (Grudd and Schneider, 1996). Maps of the ice surface are available for the years 1949, 1959, 1969, 1980 and 1990 (Holmlund, 1996). The most recent map of bed topography was made by Herzfeld et al. (1993). Radar soundings of the CTS depth were conducted in 1989 (Holmlund and Eriksson, 1989) and 2001 (Pettersson et al., 2003). The polythermal structure of Storglaciären was first described by Hooke et al. (1983). The dynamics of the cold surface layer was the topic of R. Pettersson's Ph.D. thesis (Pettersson, 2004), which serves as a starting point for this study.

2.3 Observations

2.3.1 Surface and Bed Topography and Position of the CTS

The following data sets build the basis of this diploma thesis (all data sets were provided by R. Pettersson):

- Bed: Herzfeld et al. (1993)
- Surface: Holmlund (1996)
- CTS: Pettersson et al. (2003)

In this study, a *kinematic center line* similar to the one described in Jansson (1997) was used for all modeling purposes. Bed and surface topography as well as the thickness of the cold layer were interpolated at 50 evenly spaced points along this flow line and smoothed afterwards (Figure 2.3).

2.3.2 Ice Velocity

A data set provided by R. Pettersson *(unpublished)* was used. Measurements were taken at the following dates:

- Lower stake net measured between 31.08.2001 and 13.07.2002
- Middle stake net measured between 14.09.2001 and 14.07.2002
- Upper stake net measured between 02.05.2001 and 05.05.2002

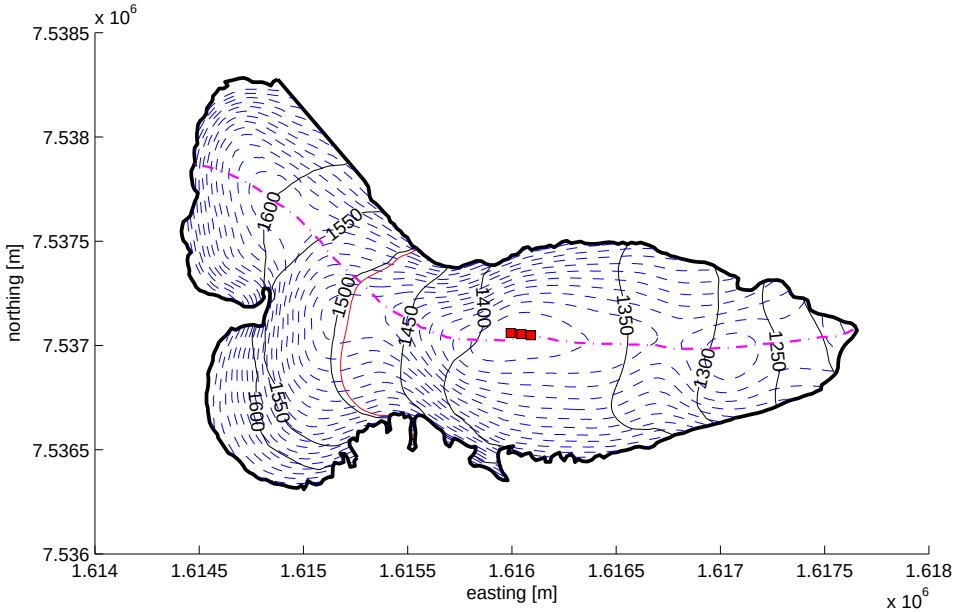

(a) Map of surface and bed topography of Storglaciären. Solid black lines and dashed blue lines indicate surface elevation (50 m contour interval) and bed elevation (20 m contour interval), respecitvely. The solid red line indicates the approximate position of the equilibrium line in 2002, the dashed-dotted magenta line is the *kinematic center line*, and red squares mark positions of thermistor strings.

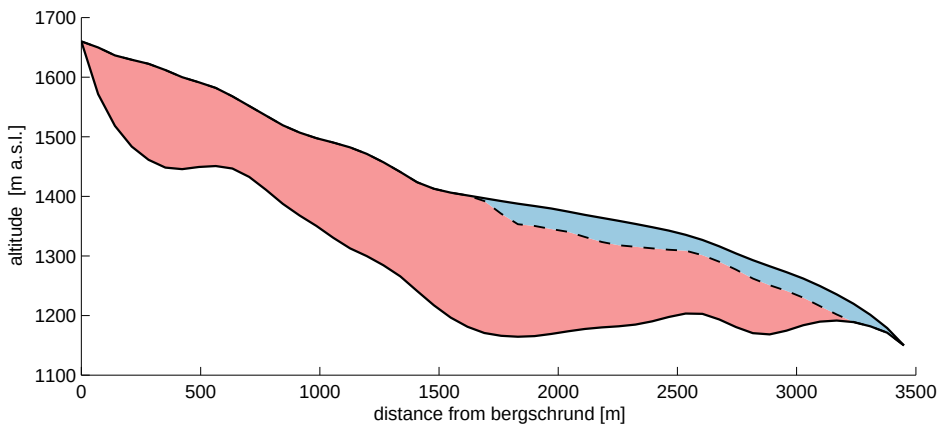

(b) x-z slice along kinematic center line of Storglaciären. The dashed line indicates the position of the transition surface between the cold and temperate layer. Blue and red indicate cold and temperate ice, respectively.

Figure 2.3: Map of Storglaciären and slice along the *kinematic center line.*

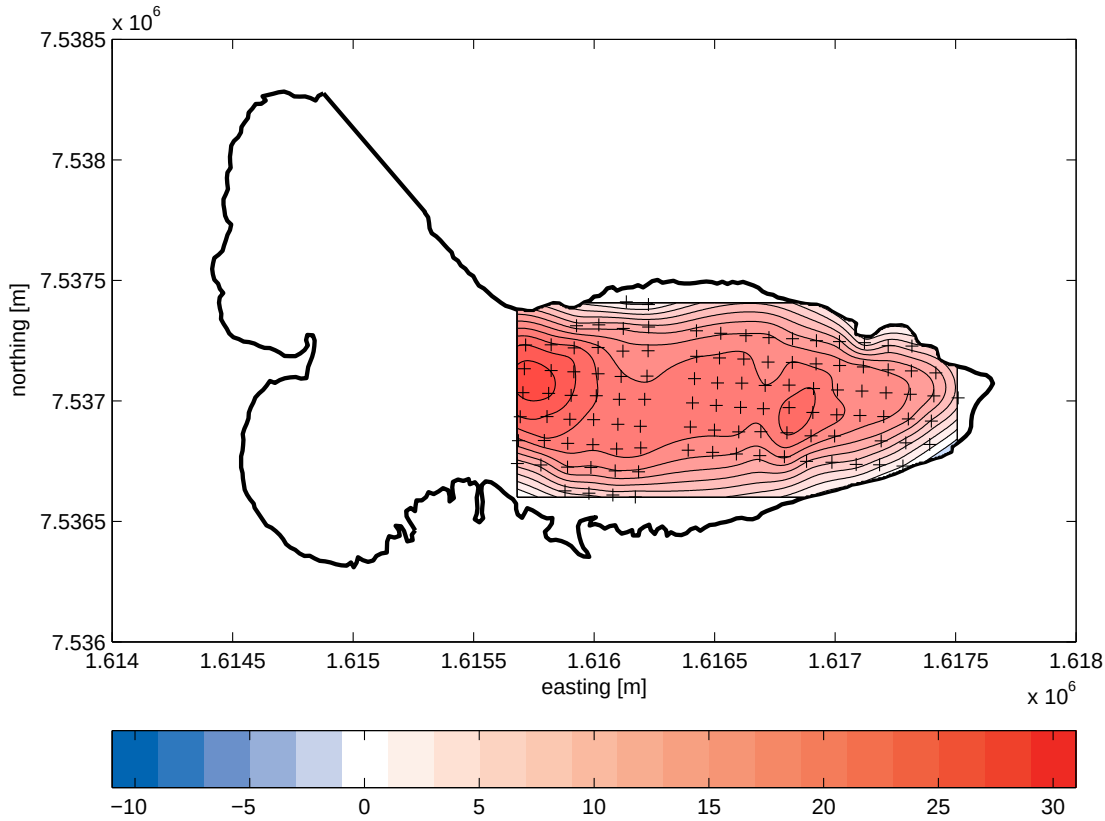

Figure 2.4: Average position of the velocity stakes (+) on Storglaciären between May 2001 and May 2002 and derived horizontal velocities. Values in meters per year. Data courtesy of R. Pettersson.

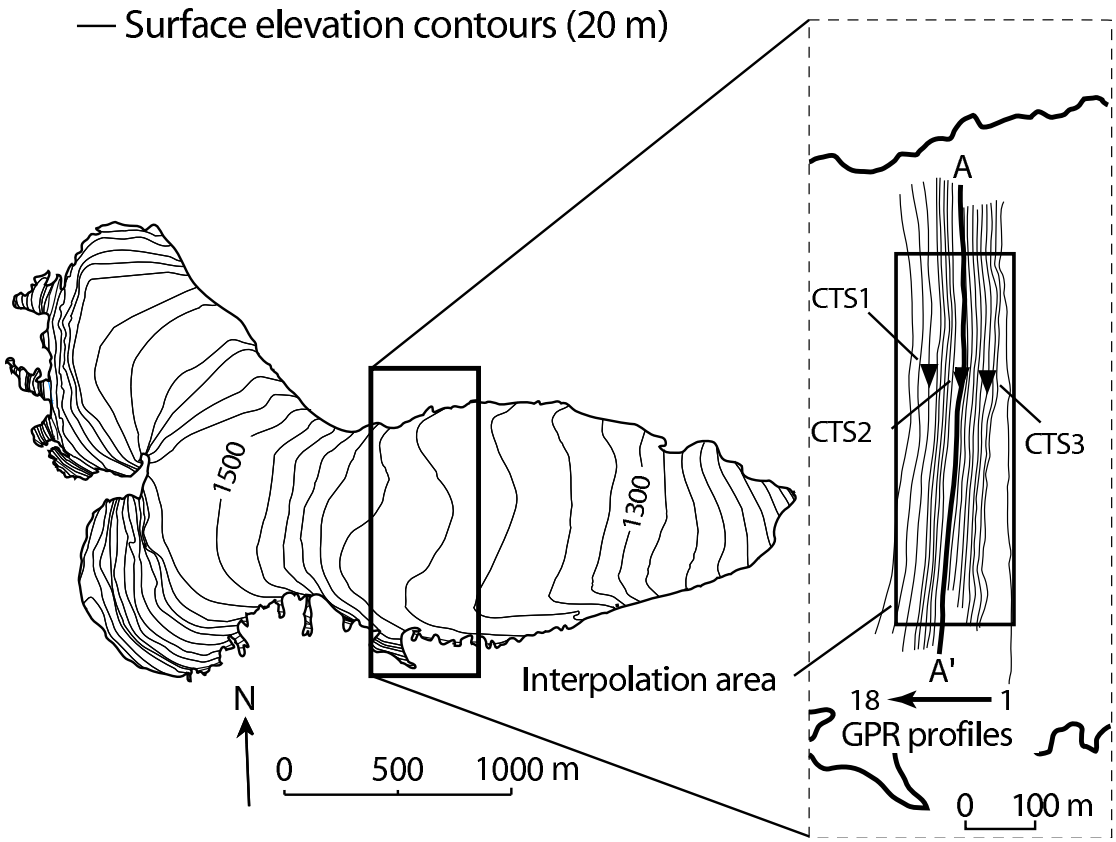

Figure 2.5: Location map for the GPR profiles. Inlet shows region of interpolated water content. CTS1, CTS2 and CTS3 are the positions of the thermistor strings. Modified after Pettersson et al. (2004). Data courtesy of R. Pettersson.

2.3.3 Water Content

The water content (or moisture content) ω is defined as:

$$\omega := \frac{\rho_w}{\rho}, \qquad \left[\frac{\mathrm{kg_w}}{\mathrm{kg}}\right] \tag{2.1}$$

where ρ_w is density of water and ρ is density of the ice-water mixture.

Pettersson et al. (2004) determined the absolute water content at three calibration points as depicted in Figure 2.3(a). The results show a water content of $0.0080\,\mathrm{kg_w/kg}$, $0.0075\,\mathrm{kg_w/kg}$, $0.0058\,\mathrm{kg_w/kg}$. 18 transverse GPR profiles were surveyed and the water content was interpolated within the studied area as shown in Figure 2.5. A mean absolute water content of $0.008\,\mathrm{kg_w/kg}$ was obtained for this area.

3 Models and Model Tests

3.1 Second Order Ice Flow Model

The mechanical model used in this study is a two dimensional, second order glacier mechanics model. It was originally developed and written by Heinz Blatter. Necessary adaptions were implemented by the author of this study. The following notation is introduced: FOA stands for *first order approximation* and SOA for *second order approximation*, describing the numerical order of the mathematical equation scheme. For details on physical and numerical properties, see Colinge and Blatter (1998) and Blatter et al. (1998). The model calculates horizontal (u) and vertical (w) velocities as well as strain heating Q. Additionally, model results were used to drive the trajectory model.

3.1.1 Governing Equations

The second order force balance is

$$\frac{\partial \tau}{\partial z} + 2\,\frac{\partial \sigma}{\partial x} = \rho g \frac{\mathrm{d}S}{\mathrm{d}x} - \frac{\partial}{\partial x}\left(\int_z^S \frac{\partial \tau}{\partial x}\mathrm{d}z'\right), \tag{3.1}$$

where τ is the deviatoric stress tensor, σ is the normal stress tensor, g is the acceleration of gravity, and $S = S(x)$ is the upper free surface. The rheology of ice is described with a relation of the form

$$\frac{\partial u}{\partial z} + \frac{\partial w}{\partial x} = 2\,F\,\tau \tag{3.2}$$

$$\frac{\partial u}{\partial x} = F\,\sigma. \tag{3.3}$$

Using the following notation

$$G = \frac{1}{F}, \quad G_x = \frac{\partial G}{\partial x}, \quad G_z = \frac{\partial G}{\partial z}, \tag{3.4}$$

and substituting Equations 3.2 – 3.3 into Equation 3.1 yields:

$$G\left(2\,\frac{\partial^2 u}{\partial x^2} + \frac{1}{2}\,\frac{\partial^2 u}{\partial z^2}\right) + 2\,G_x\,\frac{\partial u}{\partial x} + \frac{1}{2}\,G_z\,\frac{\partial u}{\partial z} =$$

$$\underbrace{\rho g \frac{\mathrm{d}S}{\mathrm{d}x}}_{S_x} - \underbrace{\frac{1}{2} G \frac{\partial^2 w}{\partial x \partial z}}_{W_1} - \underbrace{\frac{1}{2} G_z \frac{\partial w}{\partial x}}_{W_2} - \underbrace{\frac{\partial}{\partial x}\left(\int_z^S \frac{\partial}{\partial x}\left[G\left(\frac{\partial u}{\partial z'} + \frac{\partial w}{\partial x}\right)\right]\mathrm{d}z'\right)}_{T} \tag{3.5}$$

W_1, W_2 and T are second order terms. The fluidity F is a function of the stress components:

$$F = F(\tau, \sigma) = F[\tau(F), \sigma(F)], \tag{3.6}$$

which can be written in the form of a non-linear equation for F:

$$\mathcal{F}(F) = 0 \tag{3.7}$$

In the case of a modified Glen's flow law (Blatter, 1995):

$$F = A \left[\left(\tau^2 + \sigma^2\right)^{\frac{n-1}{2}} + t_0^{n-1} \right], \tag{3.8}$$

the resulting equation becomes:

$$F^3 - F^2 A t_0^2 - A \left[\left(\frac{\partial u}{\partial x}\right)^2 + \frac{1}{4} \left(\frac{\partial u}{\partial z} + \frac{\partial w}{\partial x}\right)^2 \right] = 0 \tag{3.9}$$

with $n = 3$ and where t_0^2 is proportional to the inverse of the viscosity at vanishing effective stress.

Boundary Condition at the Surface:

$$\left[1 - \left(\frac{\mathrm{d}s}{\mathrm{d}x}\right)^2\right] \tau_s - 2 \frac{\mathrm{d}s}{\mathrm{d}x} \sigma_s = 0 \tag{3.10}$$

With Equation 3.2 – 3.3, Equation 3.10 becomes:

$$\left[1 - \left(\frac{\mathrm{d}s}{\mathrm{d}x}\right)^2\right] \left(\frac{\partial u}{\partial z} + \frac{\partial w}{\partial x}\right)_s - 4 \frac{\mathrm{d}s}{\mathrm{d}x} \left(\frac{\partial u}{\partial x}\right)_s = 0 \tag{3.11}$$

Boundary Condition at the Base:

Either a basal velocity $u_b = u_b(x)$ or a given sliding law can be prescibed (Colinge and Blatter, 1998). If no-slip conditions are assumed, then $u_b = w_b = 0$. In case of a sliding law, the basal shear traction τ_b, and the sliding velocity v_b, are functionally related via

$$\mathcal{F}\left(\tau_b, u_b\right) = 0. \tag{3.12}$$

Table 3.1: Model setup used for tests with a constant rate factor. u_b and u_s are basal and surface velocity, respectively. Values apply to all configurations listed in Table 3.2.

variable	description	value	unit
A	rate factor	0.07	$\mathrm{a}^{-1}\mathrm{bar}^{-3}$
u_b	basal velocity	0	ma^{-1}
u_s	surface velocity	*model output*	ma^{-1}

3.1.2 Model Description

The model is of full second order although it is designed to allow each second order term to be turned on or off seperately, for testing purposes. The relative importance of each term can then be investigated. Second order terms appear in Equation 3.5 on the right hand side only:

$$G\left(2\frac{\partial^2 u}{\partial x^2}+\frac{1}{2}\frac{\partial^2 u}{\partial z^2}\right)+2\,G_x\frac{\partial u}{\partial x}+\frac{1}{2}\,G_z\frac{\partial u}{\partial z}=S_x-W_1-W_2-T \tag{3.13}$$

S_x is the driving stress (first order) and W_1, W_2 and T are the second order terms. The model was run with 50 gridpoints ($\mathrm{N_x}$) in the x-direction and 100 gridpoints ($\mathrm{N_z}$) in the z-direction, where x is oriented downglacier and z points opposite the direction of gravity. The glacier is assumed to be temperate. This is true except for a small layer in the ablation area as discussed in Section 2.1. Tests were made using a rate factor that depends on temperature. However, results (not shown in this thesis) reveal that the influence of this temperature dependence is negligible small. Hence, the assumption of an entirely temperate glacier is reasonable.

3.1.3 Tests with a Constant Rate Factor

In order to study the performance of the ice flow model and to investigate differences between the first order and second order approximation, initial tests were carried out. A constant rate factor of $0.07\,\mathrm{a}^{-1}\mathrm{bar}^{-3}$ was used in first and second order model configuration, respectively, which is the same value as in Albrecht et al. (2000). Basal sliding was set to zero. No other assumptions were made. (Table 3.1). The second order configuration can be subdivided into five cases, thus resulting in six distinctive model configurations (Table 3.2). Convergence could not be achieved for model configuration VI. Therefore, only configurations I – V are discussed in detail below.

Table 3.2: Model configurations used for tests with a constant rate factor.

notation	included terms
I	first order scheme
II	W_1, W_2, T (full second order scheme)
III	W_1
IV	W_2
V	W_1, W_2
VI	T

Velocities

Figure 3.1 shows horizontal and vertical velocities for configurations I and II, respectively. The most striking feature is the large difference in horizontal velocity between first and full second order model configuration (see Figure 3.1(e) and Table 3.3). The second order model yields higher velocities throughout the whole glacier. The largest differences are found at the surface in a region with both steep base and surface topography. Second order results are up to $14.23\,\mathrm{ma}^{-1}$ (40.55 %) higher than first order results. A second location where remarkable differences are found is around a transverse bedrock ridge (riegel). The velocity distribution pattern is similar except for the riegel. Jansson (1997) studied the riegel and associated variations in surface velocity upstream of the riegel due to a pulling from downstream through longitudinal coupling across the riegel. Complex coupling effects are assumed to be modeled more accurately when incorporating second order terms.

The following definitions are used:

$$\Delta v_{\min} := \min\left(v_{ij}^{\mathrm{SOA}} - v_{ij}^{\mathrm{FOA}}\right) \tag{3.14}$$

$$\overline{\Delta v} := \frac{1}{ij}\sum_{j=1}^{N_z}\sum_{i=1}^{N_x}\left(v_{ij}^{\mathrm{SOA}} - v_{ij}^{\mathrm{FOA}}\right) \tag{3.15}$$

$$\Delta v_{\max} := \max\left(v_{ij}^{\mathrm{SOA}} - v_{ij}^{\mathrm{FOA}}\right), \tag{3.16}$$

where v_{ij} is either the horizontal or vertical velocity at the grid point (i, j). The mean of the differences in horizontal velocity between FOA and SOA, $\overline{\Delta u}$, is $2.04\,\mathrm{ma}^{-1}$ (13.72 %), and vertical velocity $\overline{\Delta w}$ is $-0.38\,\mathrm{ma}^{-1}$. Vertical velocities were calculated based on the integrated continuity equation $\frac{\partial u}{\partial x} + \frac{\partial w}{\partial z} = 0$:

$$w(z) = u_b\frac{\mathrm{d}b}{\mathrm{d}x} + \int_0^z \frac{\partial u}{\partial x}\mathrm{d}z', \tag{3.17}$$

where u_b is horizontal velocity at the glacier bed.

To identify the second order term, which is most likely responsible for the very high simulated velocities, horizontal and vertical surface velocities are depicted in Figure 3.2

Table 3.3: Comparison of 1st (FOA) and 2nd order (SOA) velocity fields a with constant rate factor. Values in meters per year.

	min	mean	max
u_{ij}^{FOA}	0	13.56	35.09
w_{ij}^{FOA}	-10.90	-1.39	2.05
u_{ij}^{SOA}	0	15.60	49.32
w_{ij}^{SOA}	-16.81	-2.31	3.41

	Δv_{min}	$\overline{\Delta v}$	Δv_{max}
horizontal velocity u	-1.08	2.04	14.25
vertical velocity v	-5.92	0.38	2.40

separately for all model configurations (I – V). Configuration V, with W_1 and W_2 terms combined, yields horizontal surface velocities similar to the full second order scheme over the first 500 m downglacier from the bergschrund and from a distance about 1400 m away from the bergschrund down to the glacier tongue. The region in between is characterized by lower horizontal velocities than computed by the full second order scheme. Configuration III generally gives lower horizontal velocities than the first order scheme (configuration I), thus the W_1 term is most likely not the cause of the prevailing high velocities of the full second order scheme. Incorporating only the W_2 term (configuration IV), horizontal surface velocities in the accumulation area from the bergschrund to about 1130 m downstream are much higher than the full second order model. Hence, the W_2 term is presumably responsible for the very high simulated velocities. The influence of the T term is expected to be small due to the rather small difference between configuration II and V.

Accumulation Function

The accumulation function a_f is defined as:

$$a_f = u_s \frac{\mathrm{d}s}{\mathrm{d}x} - w_s, \tag{3.18}$$

where u_s is horizontal suface velocity and w_s is vertical surface velocity. This function is the theoretically necessary mass balance distribution for a glacier, not only in global but also in local equilibrium. It should not be mistaken for the accumulation-ablation function $a_s^{\perp}$ used, for example, by Greve (1995) which is a climatic input quantity. Therefore, the elevation corresponding to the level where the accumulation function is zero indicates the modeled altitude of the equilibrium line of a glacier in equilibrium (Figure 3.3(a)) and is about 1450 m a.s.l. for FOA and SOA. The pattern is the same

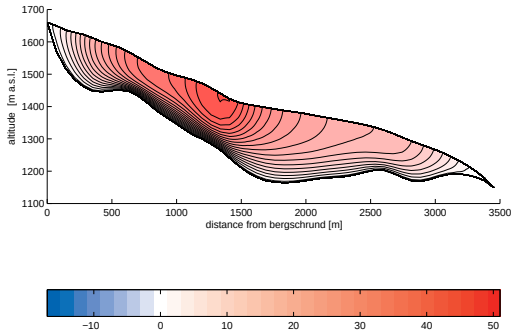

(a) 1st-order horizontal velocity u

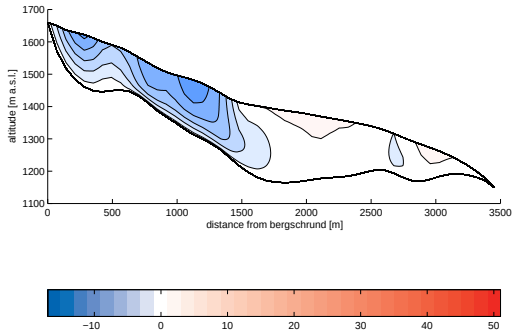

(b) 1st-order vertical velocity w

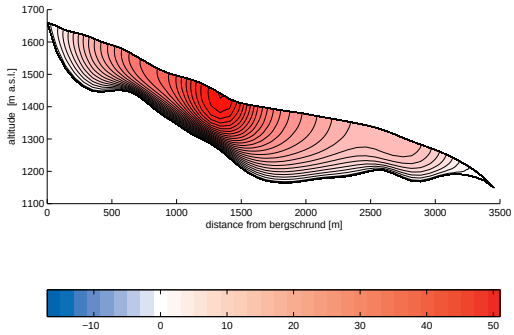

(c) 2nd-order horizontal velocity u

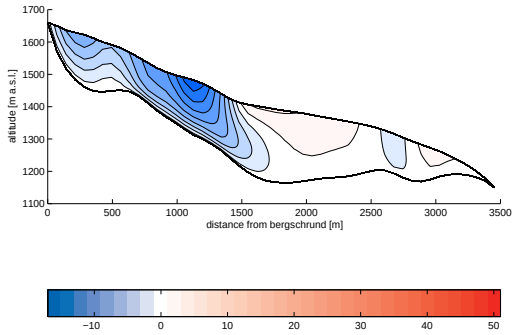

(d) 2nd-order vertical velocity w

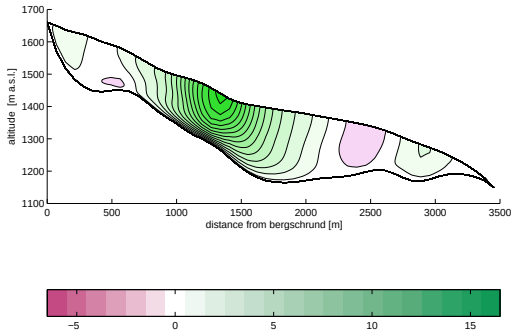

(e) Difference $2^{\text{nd}} - 1^{\text{st}}$-order horizontal velocity

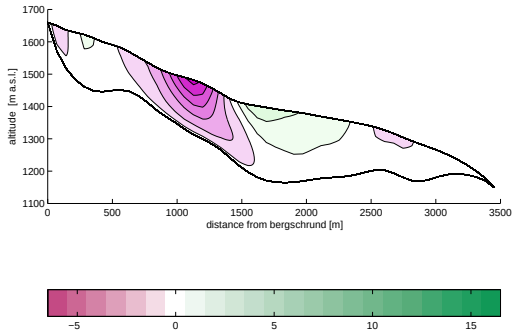

(f) Difference $2^{\text{nd}} - 1^{\text{st}}$-order vertical velocity

Figure 3.1: Comparison of 1st and 2nd order (all terms) velocity fields with constant rate factor. Contour interval in a) – d) is $2\,\text{ma}^{-1}$, in e) – f) $1\,\text{ma}^{-1}$ and values are in meters per year.

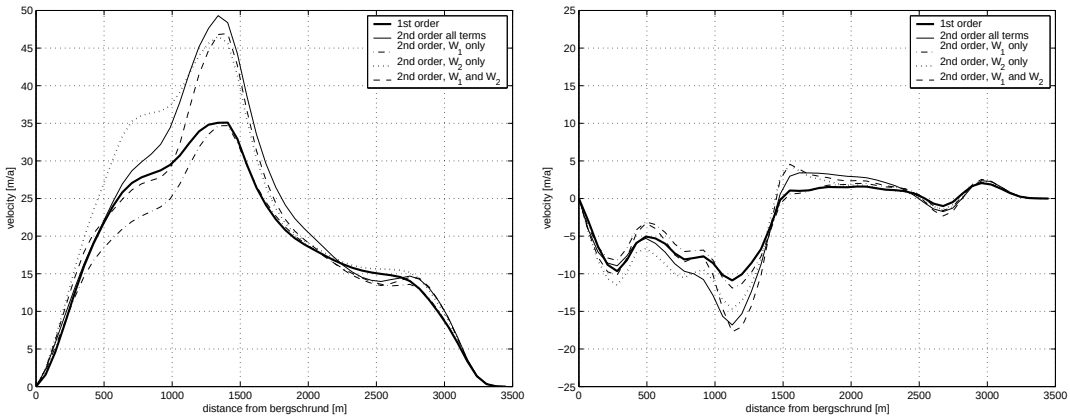

(a) horizontal surface velocities **(b)** vertical surface velocities

Figure 3.2: Surface velocities for different model configurations with a constant rate factors. The thick solid line is first order, thin solid line is full second order, dashed line includes both W terms, dashed-dotted line includes W_1 term only, dotted line includes W_2 term only. Values in meters per year.

for FOA and SOA but the amplitude of the SOA is larger. This can be understood quite easily: the accumulation function is linearly coupled with horizontal and vertical surface velocities. This result agrees with a measured altitude of the equilibrium line of 1496 m a.s.l. in 2002 (P. Jansson, personal communication 2004) since the interannual variation can be large.

Stresses

Stress fields for normal and shear stress are depicted in Figure 3.4. Also here, largest differences between FOA and SOA results can be found around the equilibrium line and below the riegel.

Surface Traction

A possible test of the model performance is to analyze the computed surface traction, which must be zero according to the surface boundary condition (Equation 3.10).

A mean surface traction of -0.0003 bar and a standard deviation of 0.0221 bar was obtained from FOA, while for SOA, a mean surface traction of -0.0049 bar and a standard deviation of 0.0622 bar was found. This order of magnitude offset is largely due to three peaks (Figure 3.3(b)): one around the equilibrium line and two just below the riegel.

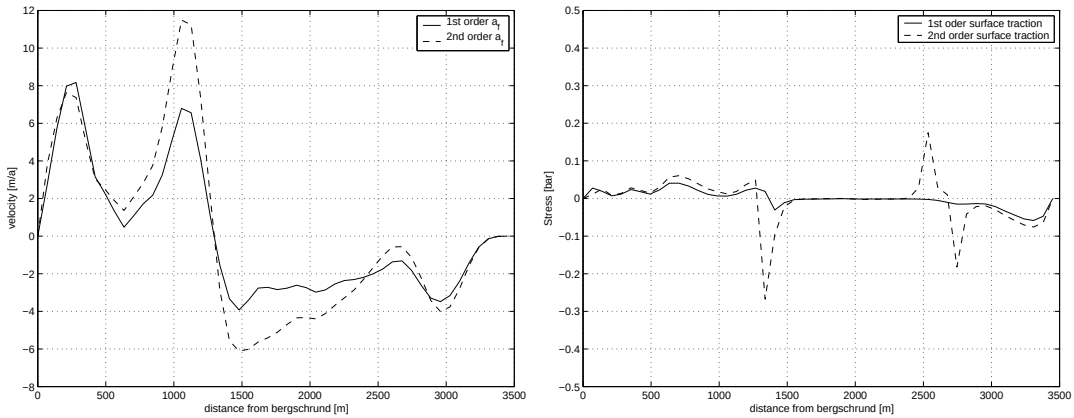

(a) Accumulation function. Solid line is 1st-order, dashed line is 2nd-order. Values in meters per year.

(b) Surface traction. Solid line is 1st-order, dashed line is 2nd-order. Values in bar.

Figure 3.3: Accumulation function and surface traction using a constant rate factor.

These two regions correspond to the regions where the highest velocity deviations occur. Discrepancies in the second order model code, especially in the formulation of the boundary conditions, is assumed to be the main cause of the weaker performance compared to the first order results. The first order code has already been thoroughly tested (H. Blatter, personal communication, 2004) and is assumed to be error-free, whereas the program code for the second order scheme is novel and not yet fully tested. Revision of the code is an important issue that should be addressed in future work with the model.

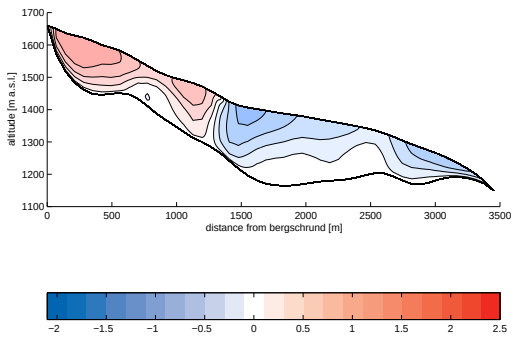

(a) 1st-order normal stress σ

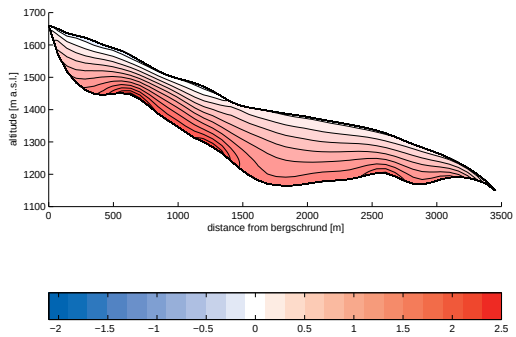

(b) 1st-order shear stress τ

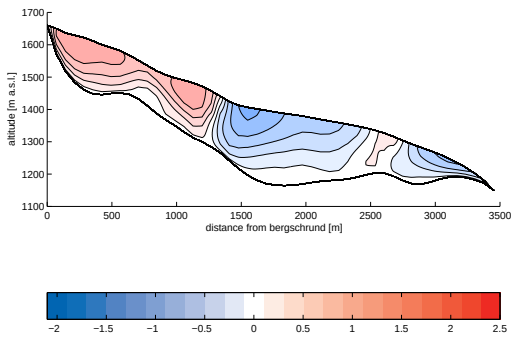

(c) 2nd-order normal stress σ

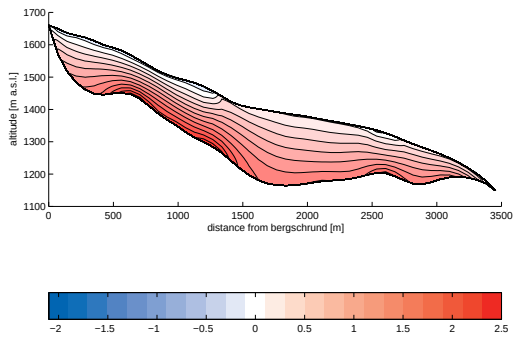

(d) 2nd-order shear stress τ

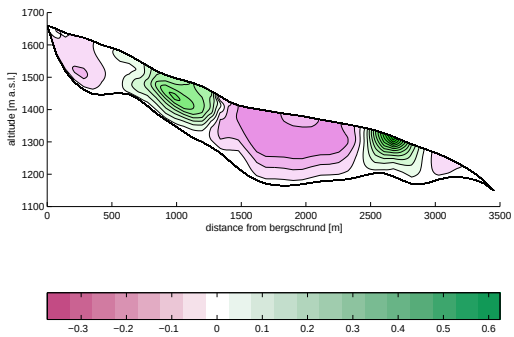

(e) Difference $2^{nd} - 1^{st}$-order normal stress

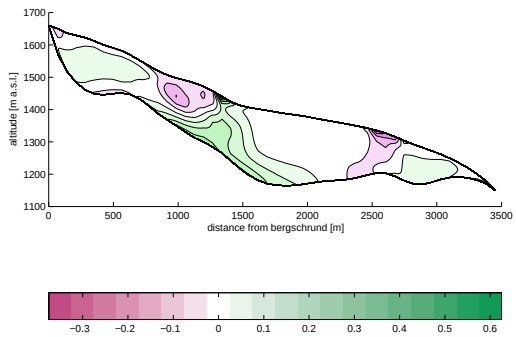

(f) Difference $2^{nd} - 1^{st}$-order shear stress

Figure 3.4: Comparison of 1st and 2nd order (all terms) stress fields with a constant rate factor. Contour interval in a) – d) is 0.2 bar, in e) – f) 0.05 bar and values are in bar.

3.1.4 Tests with Prescribed Basal and Surface Velocity

Kuriger (2002) calculated trajectories for Storglaciären based on a three-dimensional velocity field without basal sliding. This led to unrealistic results which were attributed to deficiencies of the interpolation tool or of the flow model. Kuriger also found poor correspondence between measured and modeled surface velocities and identified the assumption of no basal motion as the crucial limitation.

To overcome this, a new approach was chosen. The model was tuned in view of simulating a velocity field as close to observed data as possible. Thus, an novel iterative tuning procedure was applied.

The rate factor A is assumed to depend on physical properties of the ice such as temperature, pressure, water content, crystal size and orientation, impurities and density (Paterson, 1994). In the two-dimensional case, the rate factor is rather a tuning parameter because it is inseparably coupled with the *shape factor* (Nye, 1965). The rate factor is therefore presumed to depend on the numerical order of the model scheme as well. Values given in Paterson (1994) are suitable if the shallow ice approximation is applied, and those values used by Albrecht et al. (2000) or Gudmundsson (1999) are based on FOA and three dimensions. The rate factor is the only variable parameter of the model suitable to serve as a tuning parameter.

Boundary Conditions

Surface velocity data from observations between 2001 and 2002 were only available in the ablation zone at altitudes below 1400 m a.s.l.. There are two main reasons why velocity measurements in the accumulation zone are sparse. First, the glacier surface is steeper and much more crevassed which makes it difficult and dangerous to place velocity stakes and measure their position. Second, the proximity of rock walls shade the satellite signal used for differential GPS measurements. Hooke et al. (1989) have made a few measurements up to an altitude of 1500 m a.s.l.. An assimilation and combination of the 2001/2002 data, the measurements by Hooke et al. (1989), and model results by Jansson (1997), has provided a first estimation of surface velocities which was used as an upper boundary condition.

Knowledge of basal topography and measurements of basal velocities of glaciers is one of the key problems in glaciology. For Storglaciären, bed topography is relatively well known from radar profiles made by Herzfeld et al. (1993), but information about basal sliding is rare and high spatial variability makes extrapolation from measured points questionable. Jansson (1997) derived a basal velocity boundary condition through tuning the basal velocity until calculated surface velocities matched measured surface velocities. Although this leads to a basal velocity that works fine with the model, the number of possible solutions is still infinite (P. Jansson, personal communication, 2004). His boundary condition served as a first guess in this study and was improved through

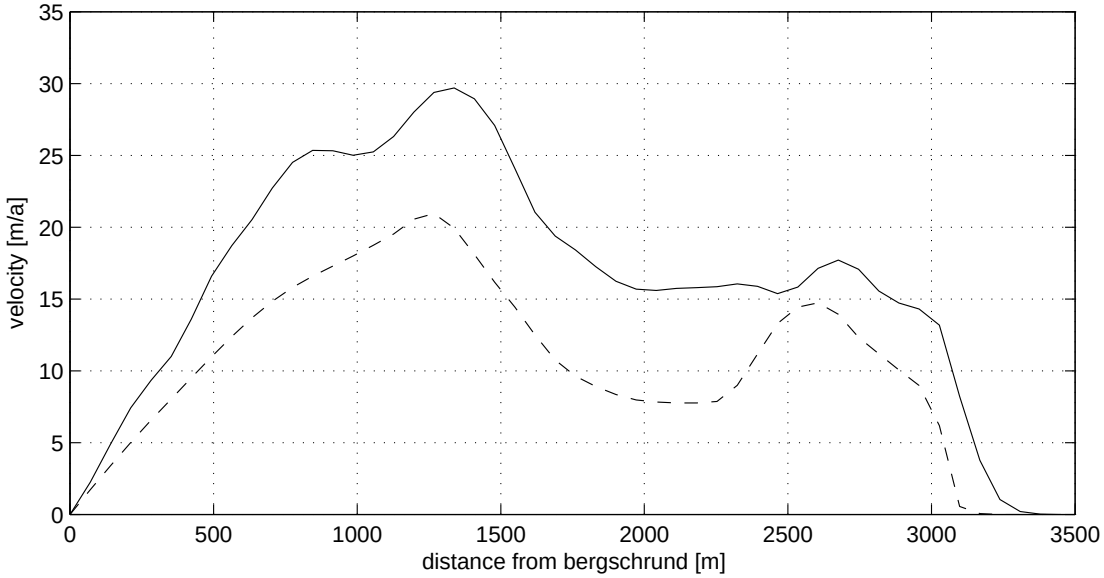

Figure 3.5: Prescribed basal and surface boundary conditions. The solid line is the surface velocity boundary condition and the dashed line is the basal velocity boundary condition. Values in meters per year.

Table 3.4: Model setup used for tests with prescribed basal and surface velocities. u_b and u_s are basal and surface velocity, respectively. Values apply to both first order and second order.

variable	description	value	unit
A	rate factor	*iteratively calculated*	$\mathrm{a}^{-1}\mathrm{bar}^{-3}$
u_b	basal velocity	*prescribed*	ma^{-1}
u_s	surface velocity	*prescribed*	ma^{-1}

a tuning and assimilation procedure described in detail below. It was decided to estimate the basal velocities and the surface velocities based on the observations and model results mentioned above. These estimations serve as an upper and lower boundary condition (from now on refered to as *prescribed surface velocity* and *prescribed basal velocity*, respectively). See Figure 3.5 and Table 3.4.

Tuning Procedure

The boundary conditions mentioned above were imposed and the rate factor was allowed to change in the longitudinal direction. After a first initialization run with $A_i^{(1)} = 0.07\,\mathrm{a}^{-1}\mathrm{bar}^{-3}$ with $i = 1, \ldots, \mathrm{N_x}$, new rate factors were calculated comparing measured and prescribed surface velocities, thus defining a fixed point iteration scheme:

Table 3.5: Comparison of 1st-order (FOA) and 2nd-order (SOA) velocity fields with prescribed basal and surface velocity. Values in meters per year.

	min	mean	max
u_{ij}^{FOA}	0	14.63	29.30
w_{ij}^{FOA}	-9.69	-2.04	4.76
u_{ij}^{SOA}	0	14.52	29.55
w_{ij}^{SOA}	-9.47	-2.03	4.70

	Δv_{min}	$\overline{\Delta v}$	Δv_{max}
horizontal velocity u	-1.54	-0.11	0.54
vertical velocity w	-0.89	0.01	0.67

$$A_i^{(l+1)} = A_i^{(l)} \cdot \frac{v_i}{u_i} \tag{3.19}$$

where u_i and v_i are the calculated and prescribed surface velocity at the ith grid line, respectively, and l is the number of the iteration step. 50 iterations were performed. Results showed an unrealistically high rate factor ($\mathrm{A} > 0.1\,\mathrm{a}^{-1}\mathrm{bar}^{-3}$) at one grid line. To avoid this, a threshold of $0.1\,\mathrm{a}^{-1}\mathrm{bar}^{-3}$ was set and a second iteration process was started. The rate factor exceeding this threshold was compensated by increased basal sliding in the following way:

$$v_b^{l+1} = v_b^l + 0.1\left(v_b^l - u_s\right), \tag{3.20}$$

where v_b is the prescribed basal velocity and u_s is the calculated surface velocity. A relaxation factor of 0.1 helped to stabilize the model (initial tests yielded unstable performance). Again, 50 iterations were computed. The resulting basal velocity is shown in Figure 3.8(a), together with the longitudinal variation of the rate factor.

This tuning process was applied to the first and the second order model. A perfect match of prescribed and calculated surface velocities was not possible to obtain, nevertheless, results are close enough for the purpose of this study since the error in estimating the basal and surface velocity boundary condition is much larger. The mean difference between SOA and FOA in horizontal velocity is $-0.11\,\mathrm{ma}^{-1}$ and in vertical velocity $0.01\,\mathrm{ma}^{-1}$ (Table 3.5). These differences are small and thus, it makes no sense to discuss model performances in detail. Nonetheless, both velocity fields were used to calculate trajectories in Section 3.2.2. Trajectories seem suitable to highlight differences in the velocity fields. For the sake of completeness, results from both orders are given in Figures 3.7 – 3.10 and Table 3.5.

Figure 3.6: Prescribed basal and surface boundary conditions as well as rate factors after the tuning process. The solid line is the surface velocity boundary condition, the dashed line is the basal velocity boundary condition and the dotted line is the rate factor. Velocities in ma^{-1}, rate factor is in $\mathrm{a}^{-1}\mathrm{bar}^{-3}$.

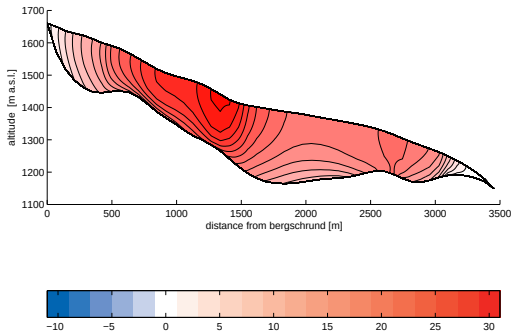

(a) 1st-order horizontal velocity u

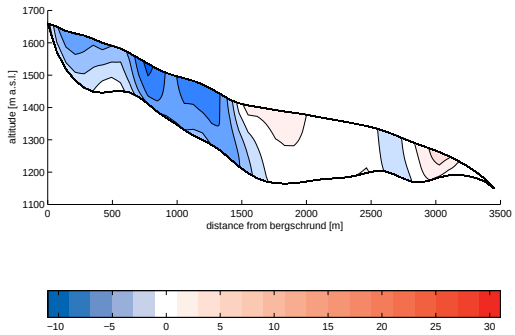

(b) 1st-order vertical velocity w

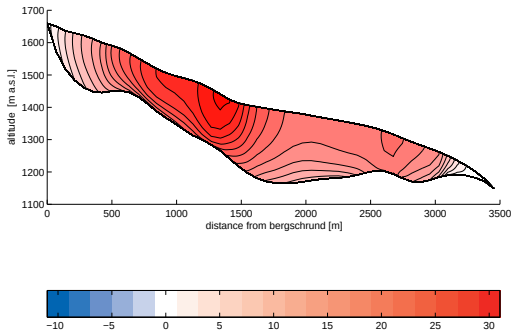

(c) 2nd-order horizontal velocity u

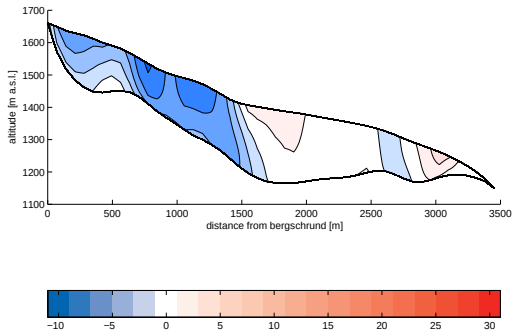

(d) 2nd-order vertical velocity w

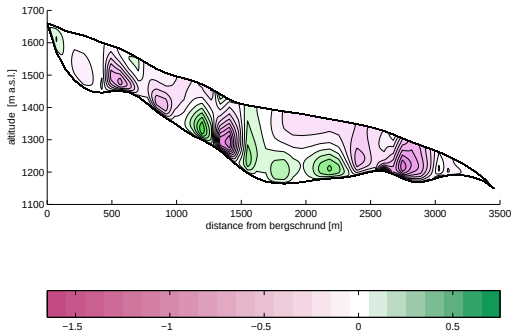

(e) Difference $2^{\text{nd}} - 1^{\text{st}}$-order horizontal velocity

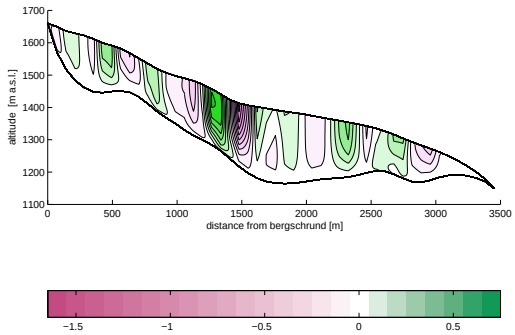

(f) Difference $2^{\text{nd}} - 1^{\text{st}}$-order vertical velocity

Figure 3.7: Comparison of 1st and 2nd order (all terms) velocity fields with prescribed basal and surface velocity. Contour interval in a) – d) is $2\,\text{ma}^{-1}$, in e) – f) $0.1\,\text{ma}^{-1}$ and values are in meters per year.

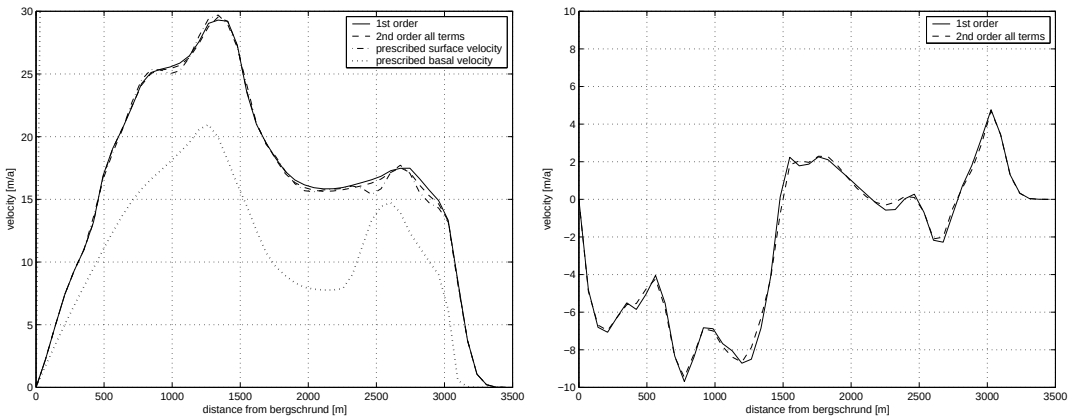

(a) horizontal surface velocities **(b)** vertical surface velocities

Figure 3.8: Surface velocities for different model configurations with prescribed basal and surface velocity. The solid line is first order, the dashed line is full second order, dashed-dotted line is prescribed surface velocity, and dotted line is prescribed basal velocity. Values in meters per year.

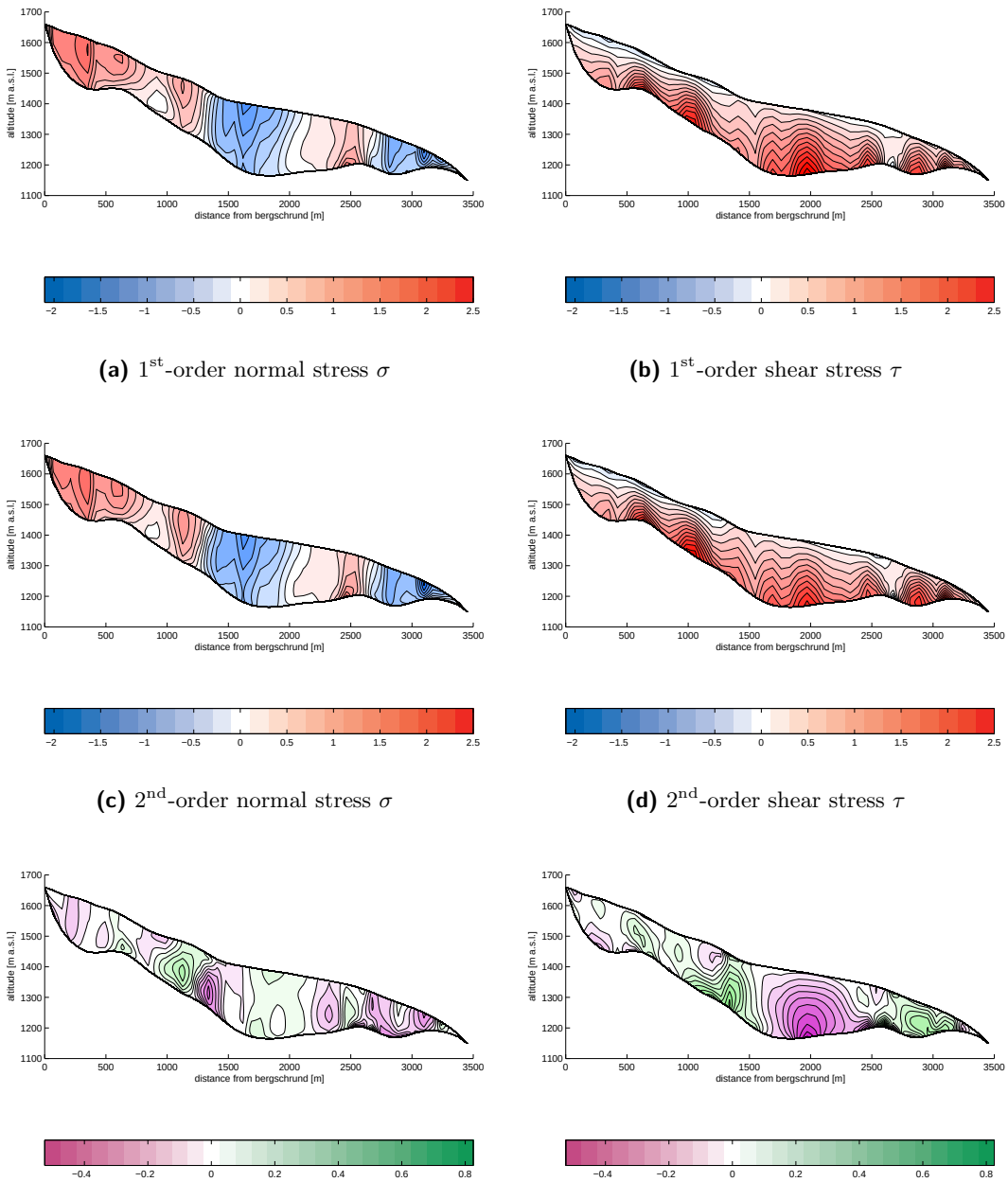

(a) 1st-order normal stress σ

(b) 1st-order shear stress τ

(c) 2nd-order normal stress σ

(d) 2nd-order shear stress τ

(e) Difference $2^{nd} - 1^{st}$-order normal stress

(f) Difference $2^{nd} - 1^{st}$-order shear stress

Figure 3.9: Comparison of 1st and 2nd order (all terms) stress fields with prescribed basal and surface velocity. Contour interval in a) – d) is 0.2 bar, in e) – f) 0.05 bar and values are in bar.

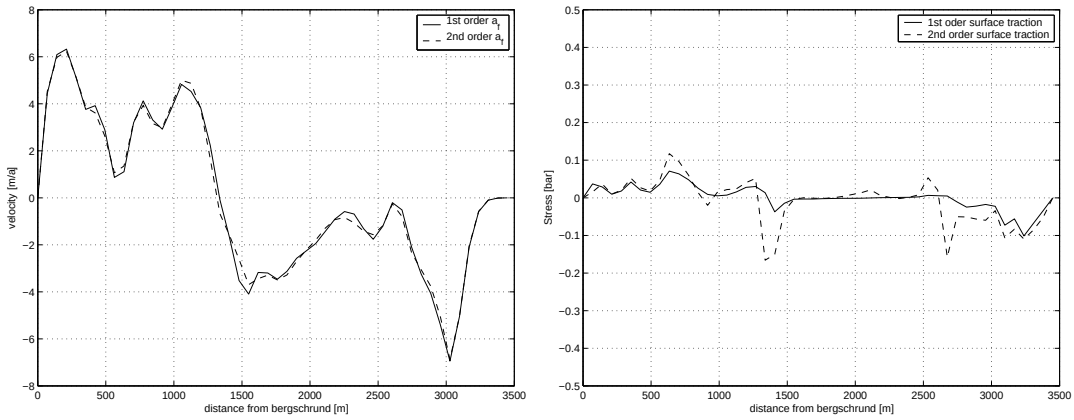

(a) Accumulation function. Solid line is 1st-order, dashed line is 2nd-order. Values in meters per year.

(b) Surface traction. Solid line is 1st-order, dashed line is 2nd-order. Values in bar.

Figure 3.10: Accumulation function and surface traction using prescribed basal and surface velocity. Values in meters per year and in bar, respectively.

3.2 Trajectory Model

3.2.1 Model Description

This section is courtesy of H. Blatter (personal communication, 2004). Given is the veloctiy field $\boldsymbol{v} = \boldsymbol{v}(\boldsymbol{r})$, where $\boldsymbol{r} = \overrightarrow{OP}$ points to the location $P(x, y, z)$. The starting point of a particle is $P(x, y, z)$ with the location vector $\boldsymbol{r}_0 = \overrightarrow{OP_0}$ at the time t_0. The trajectory of the particle follows the differential equation

$$\frac{\mathrm{d}\boldsymbol{r}}{\mathrm{d}t} = \boldsymbol{v} \tag{3.21}$$

A numerical solution of the differential equation 3.21 uses a forward Euler iteration scheme, sometimes called Petterssen iteration (Seibert, 1993):

$$\text{inital step:} \qquad \boldsymbol{r}_1 = \boldsymbol{r}_0 + \Delta t\, \boldsymbol{v}(\boldsymbol{r}_0, t_0) \tag{3.22}$$

$$\text{iteration step:} \qquad \boldsymbol{r}_{i+1} = \boldsymbol{r}_0 + \frac{\Delta t}{2}\left[\boldsymbol{v}_0 + \boldsymbol{v}(\boldsymbol{r}_i, t_0 + \Delta t)\right]. \tag{3.23}$$

If $N = 2$, this scheme is called a predictor corrector scheme. The Petterssen iteration scheme is a fixed point iteration scheme of second order accuracy, which converges towards a fixed point, if it converges at all. A fixed point P_f with location vector $\boldsymbol{r}_f = \overrightarrow{OP_f}$ is defined by

$$\boldsymbol{r}_f = \boldsymbol{r}_0 + \frac{\Delta t}{2}\left[\boldsymbol{v}_0 + \boldsymbol{v}(\boldsymbol{r}_f, t_0 + \Delta t)\right], \qquad i = 1, \ldots, N. \tag{3.24}$$

3.2.2 Test of Trajectory Model

Twentytwo backward trajectories were calculated for both FOA and SOA velocity fields described in Section 3.1.4. Results from SOA are depicted in Figure 3.11. Results from FOA look similar and are not shown. Start points were evenly distributed from the onset of the CTS to the point where it reaches the bed. The length of the shortest flow line is 680 m with a travel time of 26 a, the longest is 3150 m and has a travel time of 273 a (see Table 3.6).

Table 3.6: General properties of trajectories. Four arbitrarily chosen trajectories as depicted in Figure 3.12 are compared.

		no. of trajectory			
property	unit	5	10	15	18
length of trajectory	m	1413	1975	2388	2725
travel time	a	62	99	127	158

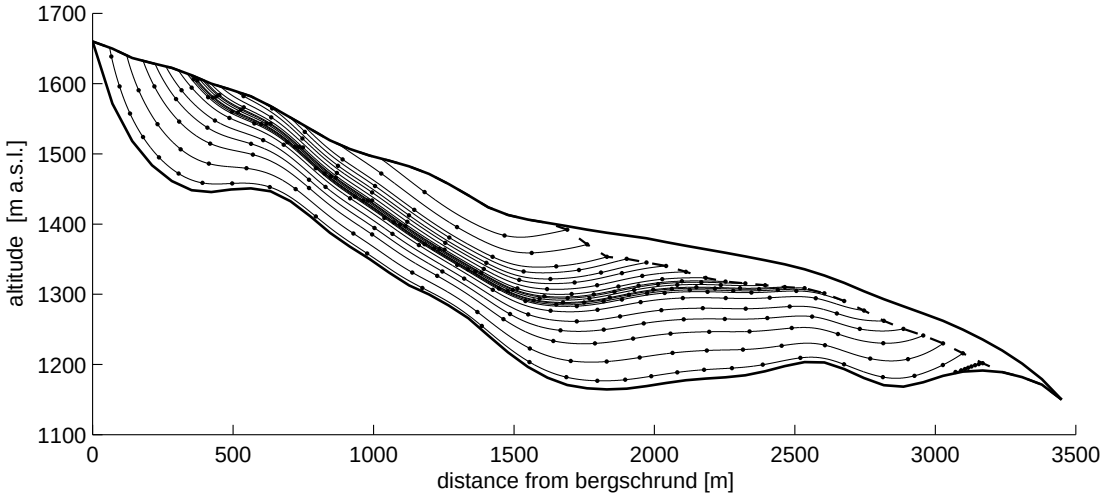

Figure 3.11: Calculated backward trajectories start at the CTS (dashed line) and are based on the SOA velocity field with prescribed basal and surface velocity and a 1d time step. Black points indicate 10a time step.

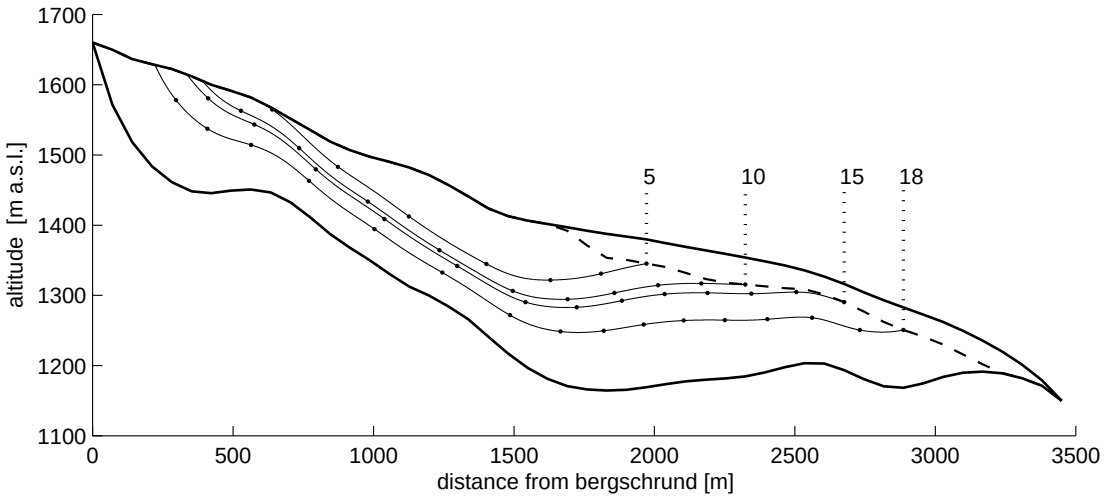

Figure 3.12: For comparison, trajectories no. 5, 10, 15 and 18 were arbitrarily chosen. Calculated backward trajectories start at the CTS (dashed line) and are based on the SOA velocity field with prescribed basal and surface velocity and a 1d time step. Black points indicate 10a time step.

Numerical Tests Four arbitrarily chosen trajectories (no. 5, 10, 15 and 18) serve as examples to investigate numerical details. Seibert (1993) associated with the Petterssen scheme a systematic phase error for purely rotational flow which leads to too slow numerically calculated trajectories. To overcome this, the time step should be chosen sufficiently small. Trajectories with a one year and a one day time step were calculated forward and backward and then compared: the difference Δx between the start point of the backward and the end point of the forward trajectory must be zero. Δx increases with increasing trajectory lengths from no. 5 to 18, but the order of the ratio between Δx and the total length l of a flow line

$$O\left(\frac{\Delta x}{l}\right) \tag{3.25}$$

is constant (10^{-3} for a 1a time step and 10^{-5} for a 1d time step). It has been decided that an error of order 10^{-5} is an acceptable compromise between accuracy and computational time. A time step of 1d was therefore used to calculate strain heating. Details are given in Table 3.7 and Figure 3.13.

Table 3.7: Numerical tests with trajectories. Four arbitrarily chosen trajectories as depicted in Figure 3.12 are compared. Values in meters.

		no. of trajectory				
order	time step	5	10	15	18	mean
difference between forward and backward						
1	1a	8.69	13.27	17.08	26.06	16.28
2	1a	8.46	12.63	16.92	24.69	15.68
1	1d	0.02	0.04	0.05	0.07	0.05
2	1d	0.02	0.04	0.05	0.07	0.05
difference between 1a and 1d time step						
1	1a,1d	20.52	6.33	8.66	9.42	11.23
2	1a,1d	31.05	5.27	6.39	9.89	13.15

Difference between FOA and SOA The end points of first and second order velocity fields were compared for a 1a and 1d time step. In both cases, the difference between FOA and SOA seems to be independent of the trajectory length l. This indicates that there is no systematic difference between first and second order fields (Table 3.8).

Test with an Alternative Basal Boundary Condition

Flow lines are very sensitive to a given flow field due to their accumulative effect. Since the basal velocity boundary condition accounts for the largest uncertainty of all assumptions and measurements applied in this study, an alternative basal velocity boundary

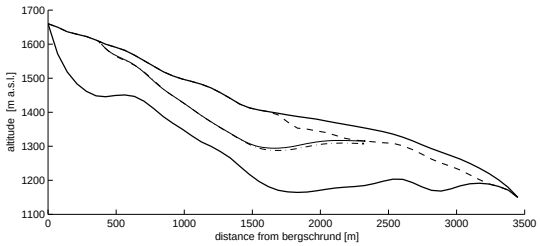

(a) 1a time step.

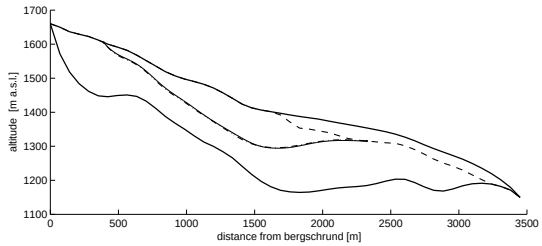

(b) 1d time step. End points are so close that the difference in position is not visible.

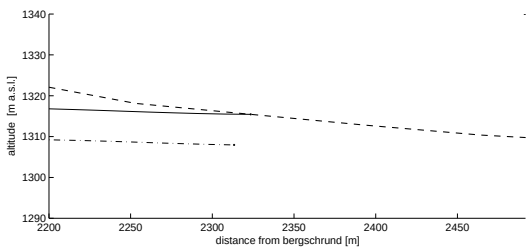

(c) 1a time step, zoomed.

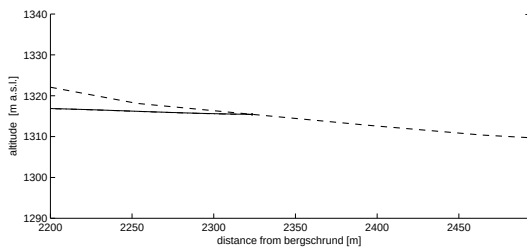

(d) 1d time step, zoomed. End points are so close that the difference in position is not visible.

Figure 3.13: Accuracy test of the forward Euler scheme. Thick dashed line is the position of the CTS, thin solid line is backward trajectory and thin dashed-dotted line is forward trajectory. Forward trajectory was started at the end position of the backward trajectory and integrated over the same time span. The end point of the forward trajectory is compared with the start point of the backward trajectory. The difference of both points gives an idea of the accuracy of the trajectory model. Trajectory no. 10 is plotted, and results from all four investigated trajectories are collected in Tables 3.7 and 3.8. This comparison is based on the second order velocity field with prescribed basal and surface velocity. Results using the first order scheme are similar (not shown).

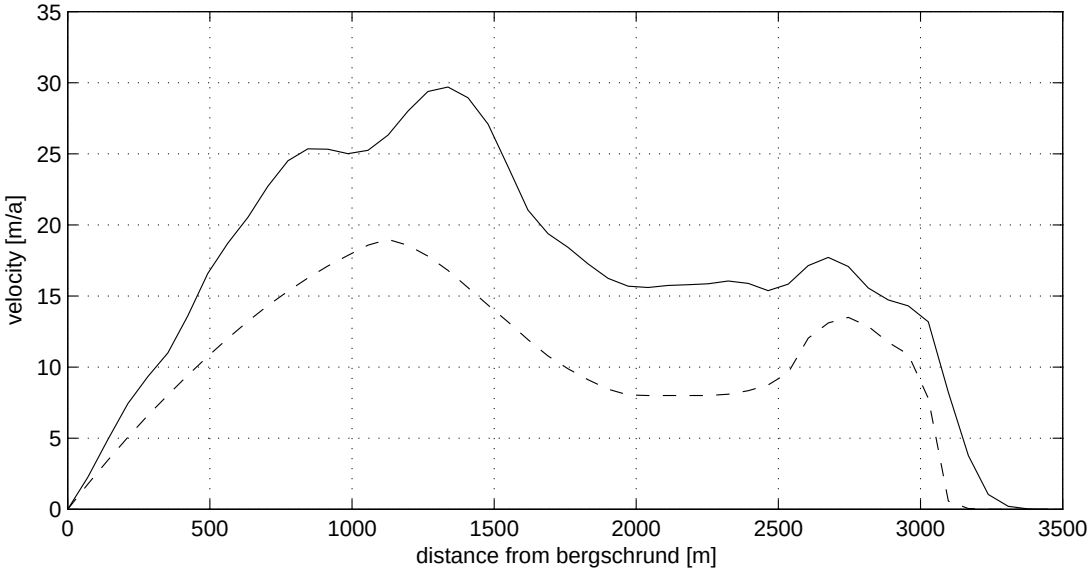

(a) Alternative basal velocity boundary condition (dashed line), the solid line is the surface velocity boundary condition which is the same as in Figure 3.5.

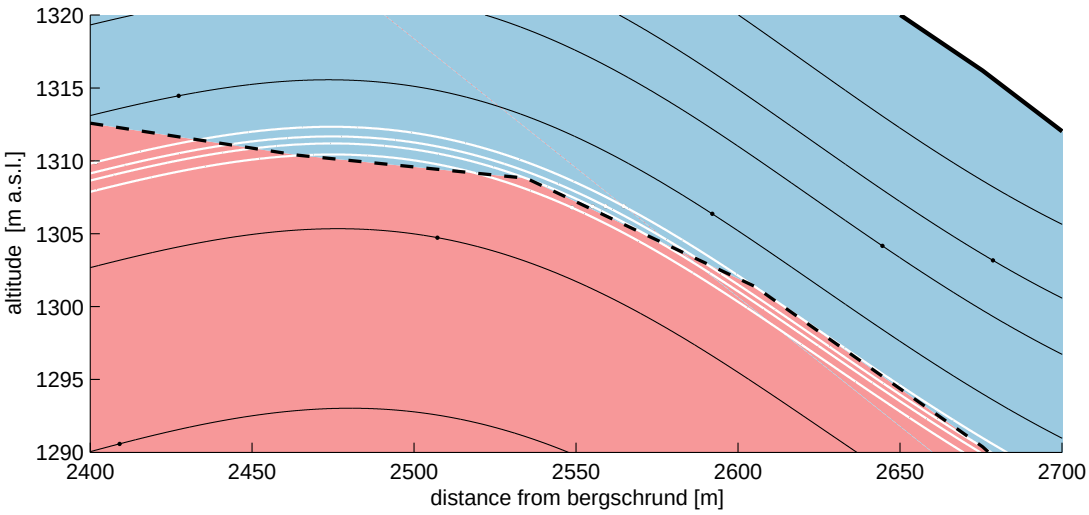

(b) Trajectories calculated using an alternative basal velocity as plotted in Figure 3.14(a). Trajectories based on SOA mechanic model and a 1d time step. Light blue indicates the cold layer and light red the temperate layer. The dashed line is the CTS. White colored trajectories flow from the temperate into the cold layer and back into the temperate. See Figure 3.15 for more information.

Figure 3.14: Tests with an alternative basal velocity boundary condition.

Table 3.8: Trajectory comparison sheet. Differences between FOA and SOA. Four arbitrarily chosen trajectories as depicted in Figure 3.12 are compared. Values in meters.

		no. of trajectory				
order	time step	5	10	15	18	mean
difference between FOA and SOA						
1,2	1a	24.22	5.07	11.32	3.37	11.00
1,2	1d	34.86	3.45	8.77	4.12	12.80

condition (Figure 3.14(a)) was tested with the SOA model and 1d time step trajectories. Figure 3.14(b) reveals a surprising feature. The topography of the CTS in conjunction with the flection of certain trajectories entails flow lines almost parallel to the CTS. In addition, the CTS crosses certain flow lines two or even three times. This behavior was not expected and also not found in the literature about Storglaciären. A physical interpretation and a discussion of possible consequences is given below.

The CTS is defined by a change in temperature. Ice is below the pressure-corrected melting point on the cold side whereas ice is at the pressure-corrected melting point on the temperate side. On the other hand, the CTS as seen by a ground-penetrating radar (GPR) is tied to a change in the water content. Until now, it was assumed that the two surfaces coincide. Flow lines, as shown in Figure 3.14(b) however, support the possible existence of a temperate, but dry region. The following processes are illustrated in Figure 3.15. The labels A, B and C correspond to the labels in this figure.

A Ice particles traveling downglacier accumulate water. When they arrive at the CTS for the first time, all liquid water freezes. Latent heat is released and transported into the cold ice because of a negative temperature gradient on the cold side (Greve, 1995). Now flowing through this cold region, ice will not accumulate water since the energy due to strain heating is not sufficient to melt ice.

B Ice passing the CTS here cannot immediately melt as Greve (1995) has shown. This is due to the fact that there is no way to transport the energy necessary for melting to the CTS. Ice flow from the cold to the temperate side is only possible if no melting at the transition surface occurs. On the temperate side, the only contribution to a negative temperature gradient originates from the pressure dependence of the melting point, which is small for a small glacier like Storglaciären. Ice in this region is temperate, but mostly dry. The water content increases only slightly along the flow lines.

C Ice with low water content crosses the CTS and once again, water freezes out and latent heat is released into the cold side. Due to the low water content, less heat is freed this time.

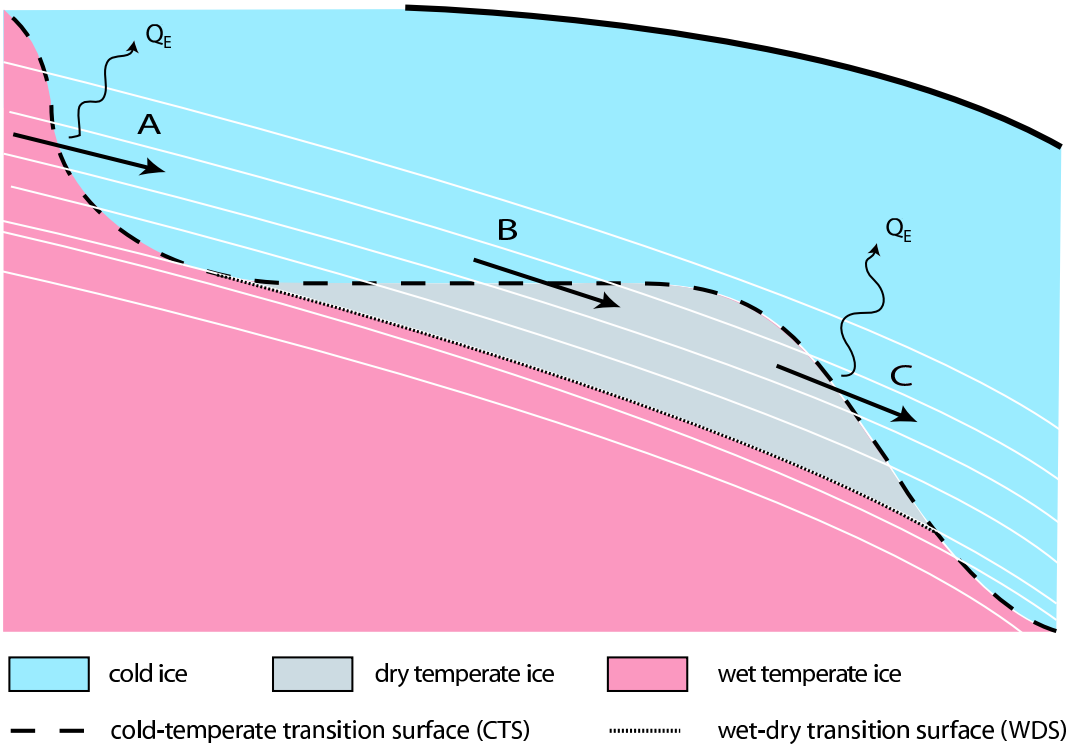

Figure 3.15: Schematic depiction of the difference between the cold-temperate transition surface and the wet-dry transition surface. Q_E is latent heat flux due to freezing water, dashed line is the CTS and dotted line is the WDS. Solid white lines are flow lines. Detailed explanations are given in the text.

Hence, three zones can be distinguished: *cold ice*, *dry temperate ice* and *wet temperate ice*. Ice entering the dry temperate zone has zero water content and the only source of water is from strain heating within that zone. The boundary between dry and wet ice shall be called *wet-dry transition surface* (WDS). Unlike the CTS, the WDS is not a boundary of phase change.

Ice flowing along trajectories just below the WDS is wet, while ice flowing just above has a negligible or at least a very small water content. It is now argued that a ground-penetrating radar would detect the WDS instead of the CTS. Thus, the depth of the cold layer could be overestimated in such regions.

4 Strain Heating and Water Content

Strain heating and water content calculations presented in this section are based on SOA and 1d time step trajectories. Results using different orders and time steps yield similar values and are not shown here.

4.1 Strain Heating

The energy balance for temperate ice is:

$$\dot{\omega} + \frac{c_p}{L}\dot{\theta} = \frac{1}{\rho}\,\mathrm{div}(\nu\nabla\omega) + \frac{\mathrm{tr}\left(\dot{\boldsymbol{\varepsilon}}\cdot\boldsymbol{\sigma}^{(d)}\right)}{\rho L}, \tag{4.1}$$

where $\dot{\omega}$ and $\dot{\Theta}$ are the total derivatives of the water content and temperature, respectively, $\dot{\boldsymbol{\varepsilon}}$ is the strain rate tensor, the deviatoric stress tensor $\boldsymbol{\sigma}^{(d)} = \sigma_{ij} - \left(\frac{1}{3}\right)\sigma_{ii}\delta_{ij}$, ν is the moisture diffusivity, c_p is the heat capacity, and L is the latent heat of melting. If heat and moisture diffusion are omitted (Blatter and Hutter, 1991) and steady state is assumed, Equation 4.1 can be rewritten as:

$$\omega = \omega_0 + \int_A^B \frac{Q}{\rho L}\,\mathrm{d}t, \qquad Q = \mathrm{tr}\left(\dot{\boldsymbol{\varepsilon}}\cdot\boldsymbol{\sigma}^{(d)}\right)$$

Then, using the incompressibility assumption $\left(\frac{\partial u}{\partial x} = -\frac{\partial w}{\partial z}\right)$, we can obtain Q the following way:

$$\begin{aligned}
Q &= tr\left(\begin{pmatrix} \dot{\varepsilon}_{xx} & \dot{\varepsilon}_{xz} \\ \dot{\varepsilon}_{xz} & -\dot{\varepsilon}_{xx} \end{pmatrix}\cdot\begin{pmatrix} \sigma_{xx}^{(d)} & \sigma_{xz}^{(d)} \\ \sigma_{xz}^{(d)} & -\sigma_{xx}^{(d)} \end{pmatrix}\right) \\
&= tr\begin{pmatrix} \dot{\varepsilon}_{xx}\sigma_{xx}^{(d)} + \dot{\varepsilon}_{xz}\sigma_{xz}^{(d)} & \cdots \\ \cdots & \dot{\varepsilon}_{xx}\sigma_{xx}^{(d)} + \dot{\varepsilon}_{xz}\sigma_{xz}^{(d)} \end{pmatrix} \\
&= 2\dot{\varepsilon}_{xx}\sigma_{xx}^{(d)} + 2\dot{\varepsilon}_{xz}\sigma_{xz}^{(d)}
\end{aligned} \tag{4.2}$$

Applying the flow law $\dot{\varepsilon_{ij}} = AF(.)\sigma_{ij}$ and using $\sigma_{xx}^{(d)} = \sigma$ and $\sigma_{xz}^{(d)} = \tau$ results in:

$$Q = 2AF(.)\sigma^2 + 2AF(.)\tau^2 \tag{4.3}$$

The ice flow model computes the strain heating $Q = Q(i, j)$ at each grid point (i, j) with $i = 1, \ldots, \mathrm{N_x}$ and $j = 1, \ldots, \mathrm{N_z}$. Then, Q is interpolated using splines at all points $Q(l)$ for $l = 1, \ldots, \mathrm{N_t}$, where N_t is number of trajectory points.

4.2 Melt Water Production

The total amount of water produced due to strain heating is obtained through summing over l:

$$\omega_{cts} = \omega_0 + \frac{1}{\rho L} \sum_{l=2}^{\mathrm{N_t}} \frac{Q(l-1) + Q(l)}{2} \cdot \Delta t(l) \tag{4.4}$$

Figure 4.1(a) shows the distribution of the water content due to strain heating. The *kinematic center line* does not exactly cross the three thermistor strings but is in close proximity of less than 30 m. This allows comparison with measured data.

The water content due to strain heating along the CTS starts at 0.00039 $\mathrm{kg_w/kg}$ at the beginning of the CTS and gradually increases to maximum of 0.01143 $\mathrm{kg_w/kg}$ where the cold layer is frozen at the bed with an average value of 0.0024 $\mathrm{kg_w/kg}$ (Figure 4.1(b)).

Interpolation of the water content due to strain heating in the vicinity of the thermistor strings yields a value of 0.0006 $\mathrm{kg_w/kg}$. Pettersson et al. (2004) obtained an absolute water content of 0.008 $\mathrm{kg_w/kg}$ and associated a value of 0.001 $\mathrm{kg_w/kg}$ with strain heating. This rough estimate is very close to the value presented in this study, though it was based on several simple assumptions such as an average velocity of 17 $\mathrm{ma^{-1}}$, a maximum ice depth for flow lines of 60 m and 800 – 1000 m of horizontal lenght for the flow line. All these assumptions are close to modeled results: the maximum ice depth of the corresponding flow line is roughly the same and the flow line has a horizontal length of 1200 m, which is more than estimated, but the mean horizontal velocity is sligthly less ($\sim$ 15 $\mathrm{ma^{-1}}$, Table 3.5) than expected.

Thus, the contribution of strain heating to the observed absolute water content at the CTS is less than 10 % within the proximity of the thermistor strings. But, as Figure 4.1(a) illustrates, strain heating increases further downglacier. Due to the lack of absolute water content determinations further downstream, it is unfortunately not possible to assess if the relative contribution of melt water due to strain heating to the absolute water content at the CTS changes outside the studied area.

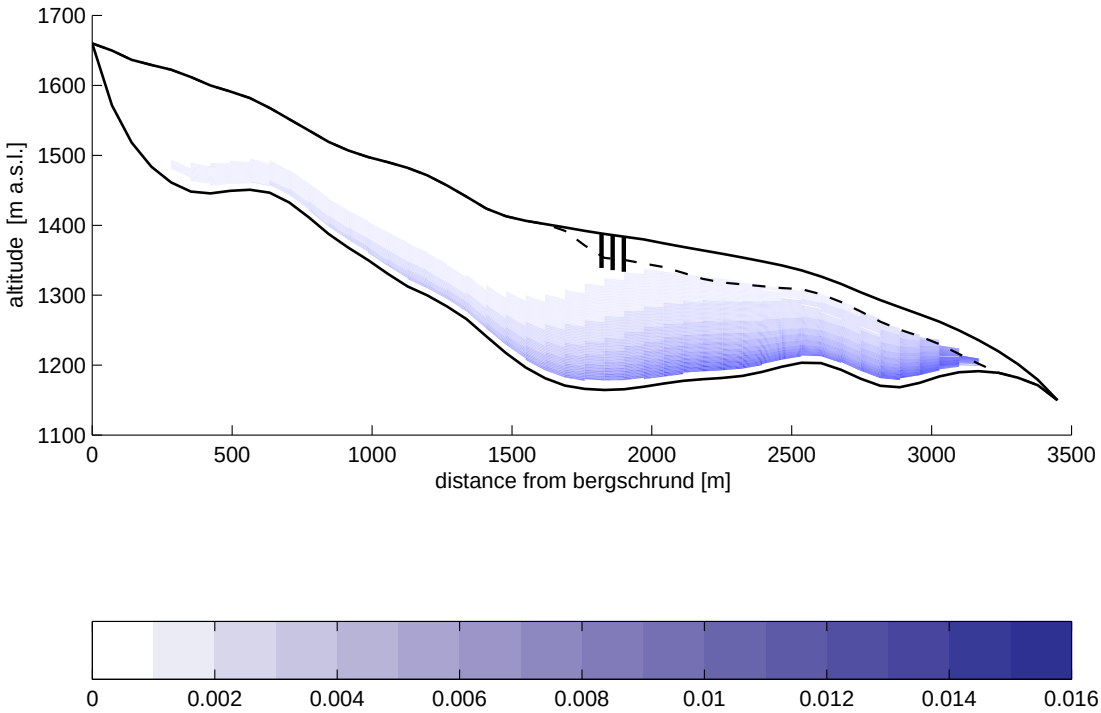

(a) Distribution of water content [kg_w/kg] due to strain heating. Solid thick lines indicate the approximate position of the three termistor strings. Plot is based on SOA and 1a time step.

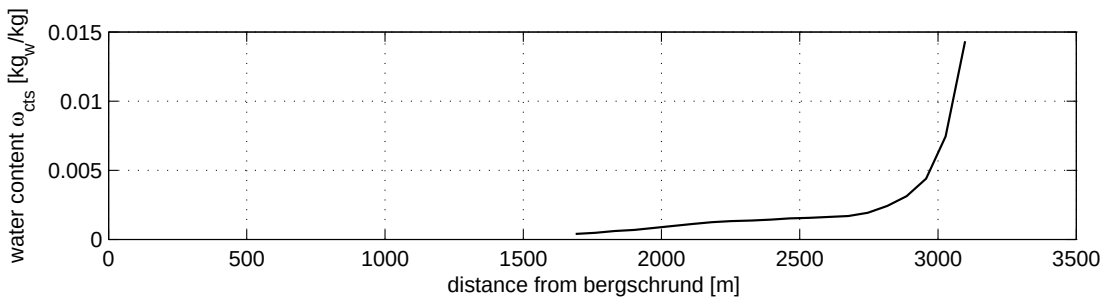

(b) Water content [kg_w/kg] along CTS due to strain heating.

Figure 4.1: Water content due to strain heating.

5 Conclusions and Prospects

The ice flow model used in this study is a fast tool to simulate velocity fields of small valley glaciers. The code of the first order scheme is reliable and has already proven its ability to simulate the flow field of Haut Glacier d'Arolla (Blatter et al., 1998) and Triftgletscher (Müller, 2004). Second order terms were introduced and results compared to the first order solution. Using the same constant rate factor, second order results reveal higher velocities throughout the whole glacier and a poorer match with the zero surface traction boundary condition (see Equation 3.10). Larger velocities are suspected to be due to a possible dependence of the rate factor on the numerical model order. The higher mean surface traction and standard deviation seems to be associated with a previously hidden error in the second order program code. Hence, the second order scheme is not yet fully verified and a thorough revision of the code is strongly recommended. Once the code is error-free, more accurate modeling of regions with steep surface and/or base topography is expected. Expansion to three dimensions and incorporating thermodynamics together with a surface evolution routine based on distributed mass balance measurements promises a challenging task for the near future.

The iterative tuning process introduced in Section 3.1.4 provides a useful method to simulate a velocity field with calculated surface velocities close to prescribed conditions. Applying the method yields first and second order velocity fields similar to each other.

It is shown that trajectories computed with a 1d time step have a negligible numerical error and no systematic difference between trajectories from first and second fields was found. Results based on the second order approximation and a 1d time step are presented, those using different orders or time steps are similiar. Tests with an alternative basal velocity condition suggest the existence of a temperate, but dry zone seperated by a *wet-dry transition surface* from wet temperate ice.

Strain heating calculated along 22 flow lines was converted into melt water production. It is concluded that the water content due to strain heating has an average value along the *cold-temperate transition surface* of $0.0024\,\mathrm{kg_w/kg}$ and in the vicinity of the thermistor strings of about $0.0006\,\mathrm{kg_w/kg}$. Pettersson et al. (2004) roughly estimated a water content due to strain heating of $0.001\,\mathrm{kg_w/kg}$ which is in good agreement with the value presented in this study.

6 Acknowledgments

First of all, I would like to thank my supervisor *Heinz Blatter* for his patience. A six week stay in Sweden was made possible due to his support. I visited Storglaciären and worked as a field assistant in order to gain practical knowledge and to counterbalance the more theoretical emphasis of my thesis. I am very grateful for all his encouragement and I am indepted to him. He answered all my (countless) questions in a calm and well considered way.

Peter Jansson and *Rickard Pettersson* for their warm welcome to Tarfala and to Stockholm University. I could greatly benefit from their knowledge. With Peter, I had my first encounter with Storglaciären and learned how to jump off a ski-doo. A thousand thanks to Rickard for his hospitality and his effort to provide all data and scripts I asked for.

At Tarfala, I got to know *Mart*, *Sara*, *Tobbe* & *Karin*. Together, we enjoyed many hours on Storglaciären and Tarfalaglaciären. With *Bob Jacobel*, I had many interersting discussions not only about glaciology. Thanks to *Regine Hock* for a marvelous helicopter flight.

Hendrik Huwald's comments helped to improve the scientific quality of this diploma thesis.

Tracy Ewen's and *Raelene Sheppard*'s careful proofreading made this thesis much more readable and comprehensible, their help is highly appreciated.

The quiet yet stimulating atmosphere in the *Diplomandenzimmer J8* helped me to focus on science. Thanks to *David*, *Christof*, *Jan* and *Roli*.

Thanks to *my family* and my good old friends *Benno, Celine, Curdin, Daniela, Grisch, Lisa & Manu & Marion, Michi, Mischi, d'Ochsä-Gang, Philipp, Pipo, Renato, Roli, Tobi, Tino, Urs & Yves* for all their support and backup during my studies.

Last, but not, least I would like to thank my study friends *Adi*, *Baptiste*, *Christian (2x)*, *Damian*, *Felix*, *Häring*, *Ingo*, *Luca*, *Luzia*, *Peter*, *Philippe*, *Ruschle*, *Simon* & *Sandro* who put up with me during the past five years. Their friendship has always been a backup, not only during our combined efforts to pass the exams.

This work is dedicated to *Boris Müller* who left us too early. I will always remember you.

Bibliography

Albrecht, O., P. Jansson, and H. Blatter (2000). Modelling glacier response to measured mass balance forcing. *Annuals of Glaciology 31*, 91 – 96.

Blatter, H. (1991). *Effect of Climate on the Cryosphere: Climatic Conditions and the Polythermal Structure of Glaciers*, Volume 41 of *Zürcher Geographische Schriften*. Geographisches Institut ETH, Zürich.

Blatter, H. (1995). Velocity and stress fields in grounded glaciers: a simple algorithm for including deviatoric stress gradients. *Journal of Glaciology 41*(138), 333 – 344.

Blatter, H., G. Clarke, and J. Colinge (1998). Stress and velocity fields in glaciers: Part II. Sliding and basal stress distribution. *Journal of Glaciology 148*, 457 – 466.

Blatter, H. and K. Hutter (1991). Polythermal conditions in Arctic glaciers. *Journal of Glaciology 37*(126), 261 – 269.

Colinge, J. and H. Blatter (1998). Stress and velocity fields in glaciers: Part I. Finite-difference schemes for higher-order glacier models. *Journal of Glaciology 148*, 448 – 456.

Fowler, A. and D. Larson (1978). Flow of polythermal glaciers: 1. Model and preliminary analysis. *Proc. R. Soc. London Ser. A-Math. Phys. Eng. Sci. 1713*, 217 – 242.

Greve, R. (1995). *Thermomechanisches Verhalten polythermer Eisschilde: - Theorie, Analytik, Numerik* -. Ph. D. thesis, Technische Hochschule Darmstadt.

Grudd, H. and T. Schneider (1996). Air temperature at Tarfala Research Station 1946-1995. *Geogr. Ann. 78A*, 115–119.

Gudmundsson, G. H. (1999). A three-dimensional numerical model of the confluence area of Unteraargletscher, Bernese Alps, Switzerland. *Journal of Glaciology 45*(150), 219 – 230.

Haeberli, W. (1976). Eistemperaturen in den Alpen. *Zeitschrift für Gletscherkunde und Glazialgeologie 11*(2), 203 – 220.

Herzfeld, U. C., M. Eriksson, and P. Holmlund (1993). On the influence of kriging parameters on the cartographic output - A study in mapping subglacial topography. *Mathematical Geology 25*(7), 881 – 900.

Holmlund, P. (1996). Maps of Storglaciären and their use in glacier monitoring studies. *Geografiska Annaler 78A*(2-3), 193 – 196.

Holmlund, P. and M. Eriksson (1989). The cold surface layer on Storglaciären. *Geografiska Annaler 71A*(3-4), 241 – 244.

Holmlund, P. and P. Jansson (2001). Glaciological Research at Tarfala Research Station. Stockholm University.

Holmlund, P., W. Karln, and H. Grudd (1996). Fifty years of mass balance and glacier front obervations at the Tarfala Research Station. *Geografiska Annaler 78A*(2-3), 105 – 114.

Hooke, L. R., P. Calla, P. Holmlund, M. Nilsson, and A. Stroeven (1989). A 3 year record of seasonal variation in surface velocity, Storglaciären, Sweden. *Journal of Glaciology 35*(120), 235 – 247.

Hooke, R. L., J. E. Gould, and J. Brozowski (1983). Near-surface temperatures near and below the equilibrium line on polar and subpolar glaciers. *Zeitschrift für Gletscherkunde und Glazialgeologie 19*(1), 1 – 25.

Hutter, K., H. Blatter, and M. Funk (1988). A model computation of moisture content in polythermal glaciers. *Journal of Geophysical Research 93*(B10), 12205 – 12214.

Jansson, P. (1997). Longitudinal coupling in ice flow across a subglacial ridge. *Annals of Glaciology 24*, 169 – 174.

Kuriger, E. (2002). Analysis of structural features in the context of measured strain rates, storglaciären, sweden. Diploma thesis, ETH Zürich.

Lliboutry, L. A. (1976). Physical processes in temperate glaciers. *Journal of Glaciology 16*(74), 209 – 218.

Maohuan, H. (1990). On the temperature distribution of glaciers in China. *Journal of Glaciology 123*(36), 210 – 216.

Müller, B. (2004). Veränderung des Triftgletschers seit 1861: Untersuchung der Stabiliätsveränderung in der Steilstufe. Diploma thesis, ETH Zürich.

Nye, J. F. (1965). The flow of a glacier in a channel of rectangular, elliptic or parabolic cross-section. *Journal of Glaciology 5*(41), 661- 690.

Paterson, W. S. B. (1971). Temperature measurements in Athabasca Glacier, Alberta, Canada. *Journal of Glaciology 10*(60), 339 – 349.

Paterson, W. S. B. (1994). *The physics of glaciers* (3. ed.). Oxford: Pergamon Press.

Pettersson, R. (2004). *Dynamics of the cold surface layer of polythermal Storglaciären, Sweden.* Ph. D. thesis, The Departement of Physical Geography and Quatenary Geology, Stockholm University.

Pettersson, R., P. Jansson, and H. Blatter (2004). Spatial variability in water content at the cold-temperate transition surface of the polythermal Storglaciären, Sweden. *Journal of Geophysical Research 109*, F02009, doi:10.1029/2003JF000110.

Pettersson, R., P. Jansson, and P. Holmlund (2003). Thinning of the cold surface layer on Storglaciären, observed by repeated ground penetrating radar surveys. *Journal of Geophysical Research 108*(F1), 6004, doi:10.1029/2003JF000024.

Seibert, P. (1993). Convergence and accuracy of numerical methods for trajectory calculations. *J. Appl. Meteorol. 3*, 558 – 566.